Materials Characterization 197 (2023) 112693

Contents lists available at ScienceDirect

Materials Characterization

journal homepage: www.elsevier.com/locate/matchar

Dynamic softening kinetics of $Al_{0.3}CoCrFeNi$ high-entropy alloy during high temperature compression and its correlation with the evolving microstructure and micro-texture

Madan Patnamsetty [a,*], Sumit Ghosh [b], Mahesh C. Somani [b], Pasi Peura [a]

[a] Materials Science and Environmental Engineering, Tampere University, 33720 Tampere, Finland
[b] Materials and Mechanical Engineering, Centre for Advanced Steels Research, University of Oulu, 90014, Finland

ARTICLE INFO

Keywords:
High entropy alloys
Critical stress/ strain
Plastic flow
Discontinuous dynamic recrystallization
Avrami equation

ABSTRACT

To establish the characteristics and kinetics of dynamic softening in a $Al_{0.3}CoCrFeNi$ high–entropy alloy (HEA), isothermal compression tests were carried out in a suitable temperature range of 1273–1423 K at 10^{-2} and 10^{-1} s^{-1} in accord with our previous study. It was found that the discontinuous dynamic recrystallization (DRX) was the dominant microstructural reconstitution mechanism. The conditions of critical stress/strain for the onset of dynamic recrystallization were determined using the Poliak–Jonas analytical criterion. Further, a kinetic model was established based on the Avrami-type function in order to be able to predict the volume fraction of DRX. The DRX volume fraction expectedly increased with strain. The microstructural investigation of the isothermally compressed specimens revealed a good agreement with the proposed DRX kinetics model and validated its accuracy. Additionally, the evolution of DRX with strain was characterized by interrupting the test carried out at 1323 K/10^{-1} s^{-1} at different strains. The progress of DRX evolving as increased formation of new recrystallized grains further corroborated the predictions of the kinetic model. The micro-texture analysis revealed random texture in the recrystallized grains, whereas the unrecrystallized grains had shown their preferred orientation towards the <101> fiber texture.

1. Introduction

The discovery of High entropy alloys (HEAs) [1] has attracted significant attention in the recent decade due to their excellent mechanical and physical properties. In addition, this alloy design concept based on the multi-principal alloying elements opens up a vast compositional space. The original concept of HEAs was to achieve a single-phase solid solution with a high configurational mixing entropy [1]. The first such development of a single-phase solid solution was the face centered cubic (FCC) CoCrFeMnNi HEA, wherein the alloying elements were in equiatomic proportions [2]. In order to further enhance the mechanical strength, a new concept of alloy design emerged that included intermetallic precipitates and multiple phases, often combining one or more alloying elements in different proportions [3]. In this context, a $Al_{0.3}CoCrFeNi$ HEA is considered as a potential engineering material for structural application due to its excellent synergy of strength and ductility [4]. Initially, the $Al_{0.3}CoCrFeNi$ HEA was assumed to have a single-phase FCC structure due to low Al concentration [5]. Whereas the as-cast $Al_{0.3}CoCrFeNi$ HEA exhibited a tensile strength of ≈300 MPa with 60% ductility, a combination of severe cold rolling to ≈90% reduction and aging at 823 K resulted in markedly enhanced tensile strength of ≈1850 MPa with a concomitant reduction of ductility to ≈5%, essentially due to the precipitation of Al—Ni based σ and B2 precipitates [6]. Recently, Wang et al. [7] reported an excellent synergy comprising tensile strength and ductility of ≈1060 MPa and ≈26%, respectively, for the $Al_{0.3}CoCrFeNi$ HEA, achieved through a cold rolling reduction of ≈70% followed by aging at 1073 K. Therefore, a careful tailoring of microstructures in $Al_{0.3}CoCrFeNi$ HEA by enabling optimized formation and stabilization of σ and/or B_2 precipitates can remarkably enhance mechanical properties, including impact toughness [8], wear resistance [9], work hardening characteristics through twinning assisted B_2 precipitation [10], and fatigue resistance [11].

High temperature mechanical processing of materials is invariably necessary to shape them into suitable components, besides imparting desired microstructures and properties. The intrinsic hot workability of an alloy depends on its chemistry, prior processing history and

* Corresponding author.
E-mail address: madan.patnamsetty@tuni.fi (M. Patnamsetty).

https://doi.org/10.1016/j.matchar.2023.112693
Received 4 September 2022; Received in revised form 22 December 2022; Accepted 16 January 2023
Available online 19 January 2023

microstructure, besides its response to the imposed deformation conditions. Processing under non-optimal temperature, strain and strain rate conditions may lead to undesirable cracking, void formation, manifestation of plastic instabilities, etc. in the microstructure. However, optimized processing based on science-based methodologies may pragmatically enable the occurrence of safe microstructural mechanisms, such as DRX and dynamic recovery (DRV), thereby preventing the formation of any microstructural defects. Therefore, it is prudent to optimize the processing conditions in order to facilitate the occurrence of safe microstructural mechanisms such as DRX, thus enabling microstructural reconstitution [12]. In a previous study by the authors [13] on the hot deformation characteristics of $Al_{0.3}$CoCrFeNi HEA, conducted in a broad matrix of different temperature and strain rate ranges, the results revealed the occurrence of various microstructural mechanisms such as manifestation of adiabatic shear bands, grain boundary (GB) cracking, flow localization and wedge cracking, depending on the deformation parameters. In addition, deformation conditions resulting in the occurrence of safe microstructural mechanisms, i.e., DRX and DRV, were also identified. The principles of dynamic materials model (DMM) were used to construct a processing map for $Al_{0.3}$CoCrFeNi HEA in order to identify various deterministic domains in the temperature–strain rate space characterizing several microstructural mechanisms that were operating in the respective domains. In addition, the instability regime marking the manifestation of unstable, localized flow resulting in microstructural defects, was demarcated on the processing map. Based on the characterization of different deterministic domains in the processing map of $Al_{0.3}$CoCrFeNi HEA [13], the deformation conditions pertaining to the domain with DRX as the dominant microstructural mechanism, was considered as ideal for the defect-free processing of $Al_{0.3}$CoCrFeNi HEA. Accordingly, the respective DRX domain of $Al_{0.3}$CoCrFeNi HEA, extending over the strain rate and temperature ranges of 2×10^{-1}–10^{-1} s^{-1} and 1273–1423 K was considered 'safe' for hot working.

It is well known that DRX is a favorable microstructural mechanism, which not only reduces the deformation resistance, but also promotes grain refinement through the microstructural reconstitution. The process, therefore, can be advantageously used during the large-scale industrial processing such as forging and hot rolling [14]. In addition, the processing parameters such as temperature, strain rate and strain, significantly influence the nucleation, size and volume fraction of the DRX grains. Therefore, it is imperative that the characteristics and kinetics of DRX are appraised to be able to understand the evolution of DRX reconstituted grains during the hot deformation processes. Also, there are limited investigations on the modelling of DRX kinetics of HEAs. For example, our previous study [15] focused on the characterization and modelling of DRX in CoCrFeMnNi HEA using the Poliak–Jonas analytical criterion and Avrami type function, investigated in the strain rate and temperature ranges of 10^{-2}–10^{-1} s^{-1} and 1223–1373 K, respectively.

The occurrence of discontinuous dynamic recrystallization (DDRX) process is the main restoration mechanism in low stacking fault energy (SFE) materials [16]. In this context, Zaddach et al. [17] reported that the SFE of CoCrFeNi HEA measured by XRD was in the range of 20–25 mJ/m^2. He et al. [18] mentioned in their study that the addition of Al in CoCrFeNi HEA lowered the SFE of $Al_{0.1}$CoCrFeNi HEA. However, recent ab initio calculations estimate the SFE of $Al_{0.3}$CoCrFeNi to be somewhat higher at ≈53 mJ/m^2 [19]. Accordingly, Gwalani et al. [20] reported formation of deformation twins in a homogenized $Al_{0.3}$CoCrFeNi following heavy cold rolling reduction of ≈90%. With regard to the high temperature deformation of $Al_{0.3}$CoCrFeNi alloy, Hagdadi et al. [21] observed the manifestation of DDRX along prior grain boundaries of the sample hot deformed at 1373 K / 5×10^{-3} s^{-1}.

It is to be noted that the desired mechanical properties can be achieved in an alloy by carefully tailoring the microstructures through optimized thermo-mechanical treatments. Nonetheless, there is a probability of micro-texture evolution during the course of hot deformation, which in turn can influence the mechanical properties. The DRX mechanism during hot deformation governs the reconstitution of the microstructure and can be associated with micro-texture evolution. In this context, they are only a few studies on the evolution of micro-texture during the hot deformation of FCC based HEAs. For example, our previous study [15] as well as that of Eleti et al. [22] on the hot deformation characteristics of CoCrFeMnNi HEA distinctly revealed the evolution of a weaker <101> fiber texture in unrecrystallized (deformed) grains along the compression axis. Further, the DRX grains showed a random texture attributing to an increase in the fraction of annealing twins (Σ3 boundaries).

In order to address different research gaps concerning the characteristics and kinetics of dynamic softening in $Al_{0.3}$CoCrFeNi HEA, the main objectives of the present investigation are:

i. to identify the critical stress/strain values for the initiation of DRX in the temperature and strain rate ranges of 1273–1423 K and 10^{-2}–10^{-1} s^{-1}, respectively, using Poliak and Jonas criterion;
ii. to establish a model elucidating the DRX kinetics at different deformation temperatures and strain rates, using an Avrami-type function;
iii. to characterize the evolution of microstructure in the course of occurrence of DRX and respective flow stress behavior and volume fraction of DRX grains, grain size and microstructural development as a function of deformation conditions;
iv. to characterize the evolution of micro-textures at different deformation temperatures and strain rates; and.
v. to understand the progression of DRX evolving with strain through interrupted testing at different strains for an appropriate test condition.

2. Experimental details

2.1. Materials and methods

An experimental casting of $Al_{0.3}$CoCrFeNi HEA, weighing ~2 kg, with the ingot dimensions of ≈140 × 40 × 40 mm was procured from Swerim AB, Stockholm. The alloy was melted in a vacuum induction melting furnace under argon atmosphere. The raw materials used were 99.9% pure elemental powders. Prior to solidification, the ingot was held in liquid state for ~1 min to ensure that complete melting and homogeneous mixing of the entire casting. The cast alloy was later soaked at 1473 K for 24 h in argon atmosphere to increase the chemical homogeneity, followed by cooling inside the furnace. Prior to hot rolling, the cast sample was preheated to 1323 K and hot rolled to ≈11 mm thickness in 26 passes with a total rolling reduction of ≈70%. The alloy was reheated in the furnace for about 10 min after every pass to maintain the rolling temperature for subsequent pass [13]. From the hot rolled plate, specimens of dimensions ≈ φ8 × 10 mm were extracted using the electric discharge machining in the traverse-normal direction, as illustrated in Fig. 1. These specimens were uniaxially hot compressed using a Gleeble® 3800 thermomechanical simulator in accordance with a test plan. Fig. 1 includes a schematic illustration of the hot compression experiments conducted in accordance with the deformation conditions pertaining to the DRX domain delineated in the processing map developed by the authors [13]. Correspondingly, the temperature and strain rate ranges of 1273–1423 K and 10^{-2}–10^{-1} s^{-1}, respectively were considered in the present work to assess and model the kinetics of DRX as a function of deformation temperature, strain and strain rate. Besides, for a select test condition (1323 K/ 10^{-1} s^{-1}) that was identified as appropriate for describing the DRX process, the samples were compressed to different strains of 0.2, 0.4 and 0.6 strains, in order to be able to characterize the progress of DRX evolving with the formation of new recrystallized grains as a function of strain. The samples were immediately cooled in air to room temperature for further characterization.

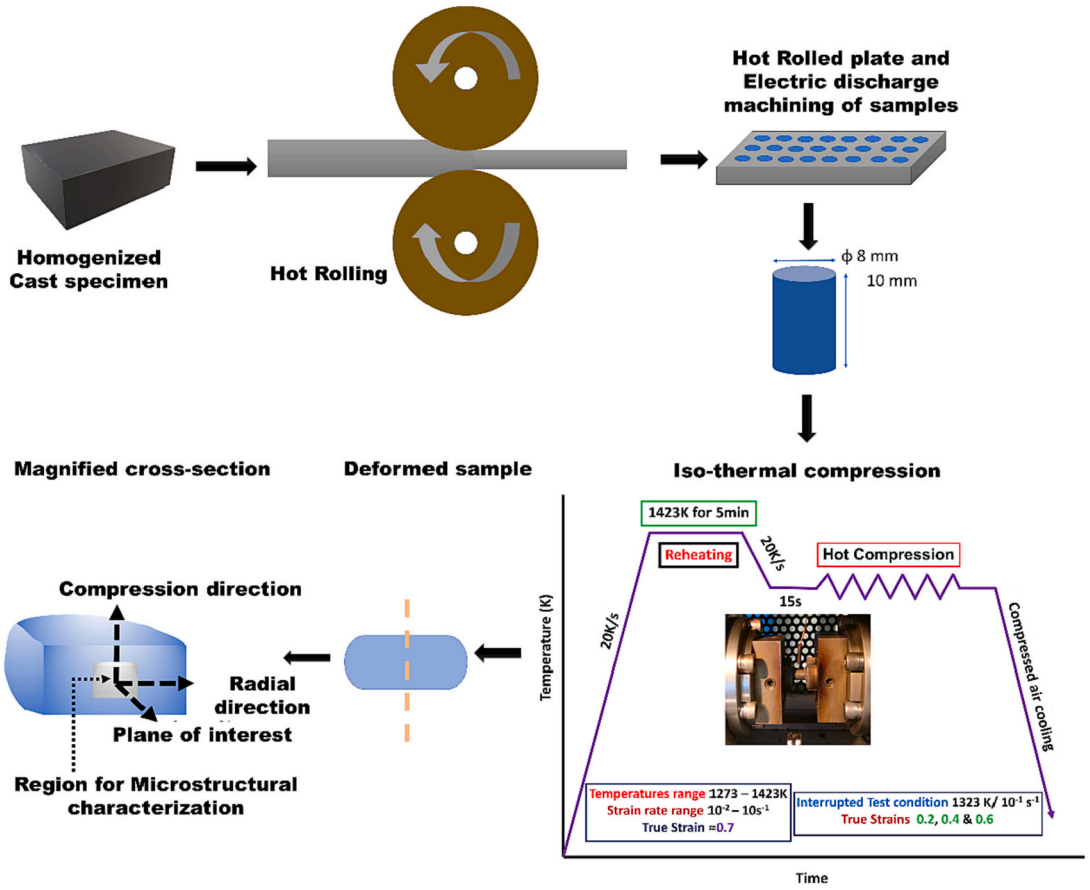

Fig. 1. A schematic representation of the experiments including hot rolling of as-homogenized $Al_{0.3}CoCrFeNi$ HEA, EDM extraction of samples, isothermal compression testing at different temperatures and strain rates using Gleeble® 3800 simulator, and finally, sectioning of the hot deformed samples along the compression axis for microstructural analysis in the plane of interest.

2.2. Material characterization

For the electron backscattered diffraction (EBSD) analysis, the hot compressed samples were polished as per the recommended procedure, the details of which are presented elsewhere [13]. A field emission scanning electron microscope (FE-SEM, Zeiss ULTRA Plus) equipped with a Symmetry® EBSD detector (Oxford instruments) was used for the acquisition of EBSD data, operated at 20 kV acceleration voltage. The location of interest for the EBSD analysis of the compressed samples is shown in Fig. 1. The EBSD data was acquired covering an area of 600 μm × 600 μm with 0.7 μm step size. Further, the HKL Channel 5 software was used to analyze the EBSD data. In order to characterize the microstructure evolution, the grain boundaries (GBs) in the EBSD maps were classified as low-angle grain boundaries (LAGBs) and high-angle grain boundaries (HAGBs) corresponding to the misorientation angle (ϕ) ranges of $2^\circ < \phi < 15^\circ$and, $\phi \geq 15^\circ$, respectively. The grains with HAGBs were considered for the grain size evaluation. Further, the Σ3 twin boundaries were disregarded for the grain size calculation. Besides, the EBSD data were used to construct the grain average misorientation (GAM) maps, in order to characterize the recrystallized, partially-recrystallized and deformed grains. In this regard, the grains with GAM values $<2^\circ$ and practically no subgrains or LAGBs inside them are regarded as recrystallized grains, while the grains with the GAM value $>2^\circ$ and mostly comprised of subgrains or LAGBs, are regarded as deformed grains. On the other hand, if the grains comprise of subgrains with the GAM value $<2^\circ$ and the misorientation between subgrains $>2^\circ$, then the grains are defined as substructured or partially-deformed grains. In addition, the Kernel average misorientation (KAM) maps were also constructed, in order to depict the local misorientation profiles in the microstructures [15].

Similarly, for the micro-texture analysis, the grains revealed in EBSD maps were grouped as recrystallized (including DRX grains) and unrecrystallized grains (including substructured grains and deformed grains) [15]. Further the pole figures were constructed for the recrystallized and unrecrystallized grains to evaluate the evolution of texture.

3. Results and discussion

3.1. Flow stress behavior

The flow curves of $Al_{0.3}CoCrFeNi$ HEA, hot deformed in the temperature range of 1273–1423 K at 10^{-2} and 10^{-1} s^{-1} strain rates are shown in Fig. 2. The flow stress values typically decrease with increase in temperature and decrease in strain rate. Further, at all the test conditions, the flow curves showed peak stress (σ_p) behavior, followed by softening of flow curves. This flow stress behavior is usually associated with the low SFE alloys that undergo hot deformation at intermediate strain rates for a possible occurrence of DRX mechanism [23]. In the early stages of compression, the flow stress increases with an increase in strain due to work hardening, which is caused by the generation and multiplication of dislocations. The flow stress values rapidly increase due to the sluggish cross slip of screw dislocations, a behavior typical of low SFE material, such as $Al_{0.3}CoCrFeNi$ HEA. The enhanced density of dislocations results in the generation of thick-walled subgrains (dynamic recovery), up to the point where the strain exceeds the critical strain (ε_c). Eventually, the DRX process sets in at a strain greater than ε_c, whereby the original strained grains are replaced by new recrystallized grains. It is assumed that the formation of DRX nuclei depends on the size of the

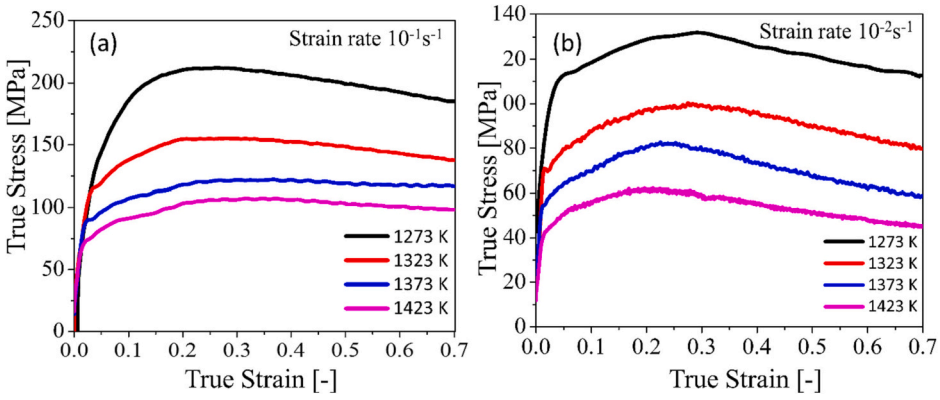

Fig. 2. Flow curves of isothermally compressed $Al_{0.3}CoCrFeNi$ HEA in the temperature range of 1273–1423 K at the strain rates of (a) 10^{-1} and (b) 10^{-2} s^{-1}.

substructured cells and the dislocations densities in the respective cell walls. Generally, the DRX flow curves are marked by flow softening beyond the peak strain (ε_p), followed by reaching a steady-state flow upon further straining. The DRX mechanism is defined as the dynamic process of nucleation and growth of newly formed strain-free grains during continued straining beyond the ε_c and is considered to be a primary softening mechanism resulting in microstructural reconstitution. Also, the average DRX grain size remains nearly constant for a given set of conditions. The presence of substructures in the DRX grains are attributed to the presence of a significant dislocation density due to the continued deformation [24]. The occurrence of DRX in the low SFE materials during continued straining is attributed to the difficulty in achieving perfect dislocations through the recombination of Shockley partials. As a result, the FCC-based HEAs have relatively low levels of cross-slip and dynamic recovery [15]. Therefore, the density of dislocations continues to increase during hot deformation particularly at high and intermediate strain rates, thereby generating a driving force for the onset of the DRX process. When the density of dislocation reaches a critical value (ε_c), the DRX process commences and the rate of work hardening begins to reduce significantly, eventually reaching the ε_p, beyond which the flow softening occurs. The flow curve softening is caused by the large-scale annihilation of dislocations because of the microstructural reconstitution via the evolution of DRX grains [25]. Eventually, the flow curve reaches the steady-state, where the work hardening process is in equilibrium with the dynamic softening process.

As mentioned earlier, the true stress-strain curves of $Al_{0.3}CoCrFeNi$ HEA samples, hot deformed in the temperature range of 1273–1423 K at 10^{-1} and 10^{-2} s^{-1}, showed typical σ_p (peak stress) behavior corresponding to the respective ε_p values (as shown in Table 1), beyond which the flow softening behavior is observed. It should be noted that the steady-state behavior could not be reached for both the strain rates and there is a continuous decrease in the flow stress up to the true strain of ≈ 0.7, which indicates the incomplete DRX process. In comparison, our previous study on the hot deformation behavior of CoCrFeMnNi HEA in the temperature range 1273–1373 K at 10^{-2} s^{-1} too showed continuous flow softening (incomplete DRX), even at the highest temperature (1373 K) [15].

Table 1
Experimental peak stress/ strain and critical stress/strain values corresponding to the manifestation of DRX in $Al_{0.3}CoCrFeNi$ HEA. Estimated $\boldsymbol{n_c}$ and $\boldsymbol{k}$ values at different test conditions are also included in the table.

Strain rate (s^{-1})	Temperature (K)	σ_c [MPa]	σ_p [MPa]	ε_c	ε_p	n_c	k
10^{-1}	1273	205	212	0.16	0.3	2.4	0.36
	1323	141	156	0.14	0.26	3.3	0.13
	1373	109	122	0.13	0.24	3.9	0.18
	1423	92	107	0.11	0.21	2.6	0.16
10^{-2}	1273	120	131	0.15	0.29	3.1	0.12
	1323	89	99	0.13	0.26	4.5	0.19
	1373	70	82	0.10	0.20	3	0.17
	1423	56	61	0.09	0.17	4.8	0.22

3.2. Identification of critical strain/stress values for the onset DRX

The method of identifying the conditions for critical strain/ stress values for the onset of DRX using the criterion proposed by Poliak and Jonas [14] has been explained in detail elsewhere [15] and is briefly described here. In this regard, the σ_c values are identified for each flow curve and the respective strain values are considered as ε_c. Further, a Fast Fourier transformation (FFT) filter was used to smoothen the flow curves, and derived with respect to strain at every strain rate and temperature, followed by determination of the strain hardening rate (θ), given as $\theta = (\partial\sigma/\partial\varepsilon)_{\dot{\varepsilon}}$ (i.e., the partial derivative of stress with respect to strain taken at constant strain rate.). Fig. 3a and b show θ *vs.* σ plots made for all the flow stress curves at the two strain rates 10^{-2} and 10^{-1}, respectively. The corresponding σ_p values were estimated corresponding to $\theta = 0$, for all the true stress-strain curves at different temperatures.

The inflection point in the θ *vs.* σ curve is defined as the σ_c for the onset of DRX [26], initially, θ slows down quickly due to the occurrence of DRV (just before the inflection point) and later, a sharp change occurs in the slope of the θ *vs.* σ curve. The green arrow as shown in Fig. 3b is the inflection point of the sample hot deformed at 1323 K/ 10^{-2} s^{-1}, representing the onset of DRX. The extrapolation of the inflection point to meet the x-axis at $\theta = 0$ illustrates the second stage, where the saturation stress (σ_{sat}) hypothetically relates to DRV. Therefore the flow softening due to DRX corresponds to the difference between σ_{sat} and σ at a particular condition of temperature and strain rate [27].

It is usually difficult to locate the exact inflection point (σ_c) from the θ *vs.* σ plot. Therefore, the inflection point is more precisely identified using an analytical approach proposed by Poliak and Jonas [14]. In this approach, the second derivative of θ *vs.* σ plot is plotted against σ value, (i.e., $\partial\theta/\partial\sigma$ vs. σ), as shown in Figs. 3(c) and (d). The σ_c is the minima of this $\partial\theta/\partial\sigma$*vs.* σ plot as shown in Fig. 3 (c), (d). Further, the ε_c values are evaluated at σ_c for each flow curve. The estimated values of σ_c, σ_p, ε_c and ε_p are listed in Table 1.

3.3. DRX kinetics

3.3.1. Strain analysis to identify the maximum dynamic softening

The strains corresponding to the maximized dynamic softening rates can be identified by plotting the work hardening rates (θ) against the strain values (ε). A representative graph showing θ *vs.* ε plots of $Al_{0.3}CoCrFeNi$ HEA at 1373 K/ 10^{-2} and 1373 K/10^{-1} is shown in Fig. 4. The dynamic softening rates are maximized at the minima of the θ *vs.* ε curves, marked as ε^* in Fig. 4. Further, the strain reaching back at $\theta = 0$ after passing the ε^* (minima) value is defined as the end of the DRX

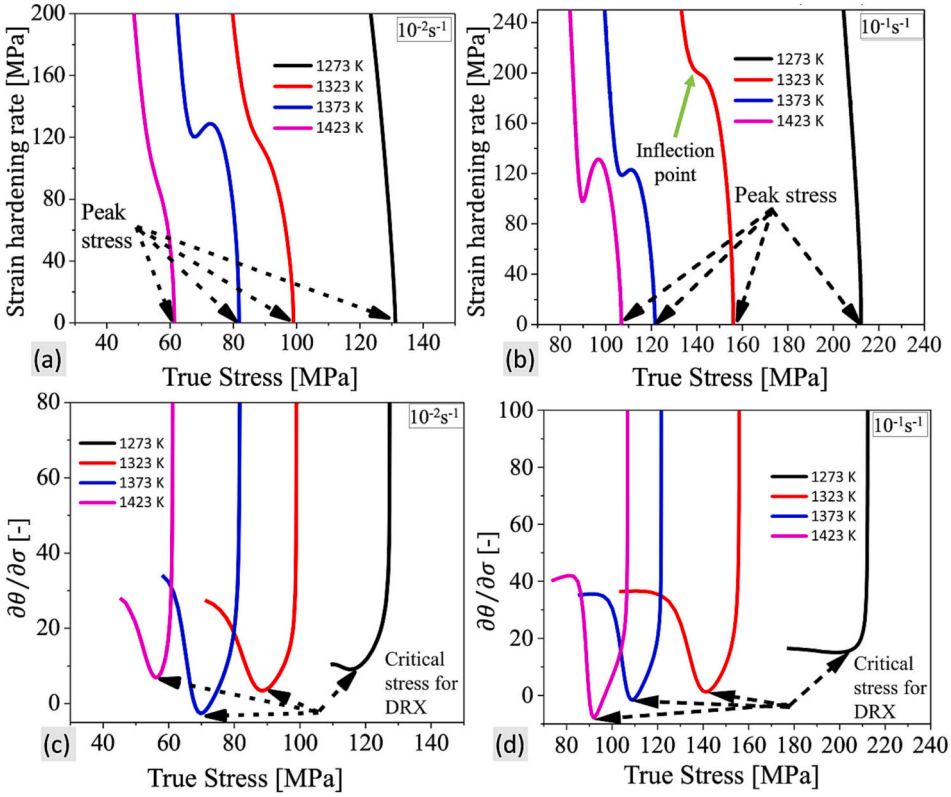

Fig. 3. Strain hardening rate vs. True stress θ *vs.* σ (a, b) and $\partial\theta/\partial\sigma$*vs.*True stress (c, d) curves of isothermally compressed $Al_{0.3}$CoCrFeNi HEA plotted at different temperatures in the range 1273–1423 K and at 10^{-2} s^{-1} (a, c) and 10^{-1} s^{-1} (b, d).

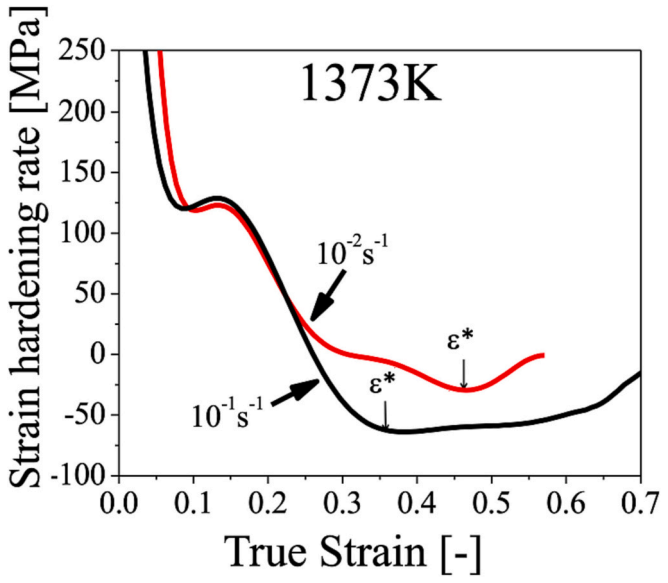

Fig. 4. Strain hardening rate (θ) vs. true strain (ε) curves for the $Al_{0.3}$CoCrFeNi HEA samples deformed at 1373 K and at two strain rates 10^{-2} s^{-1} and 10^{-1} s^{-1}.

cycle, which also marks the onset of steady-state flow. However, in some cases, the θ value doesn't return back to zero value after the minima, which represents the incomplete DRX cycle. In this case the volume fraction of DRX did not reach the maximum value, i.e., 1.

3.3.2. *Analysis of kinetic model of DRX*

In order to model the kinetics of DRX, the flow curves should exhibit σ_p behavior and flow softening on further straining. The flow curves of $Al_{0.3}$CoCrFeNi HEA samples at all the test conditions clearly exhibited work hardening at initial strains, σ_p and flow softening behaviors on further straining due to the nucleation of DRX grains. In the current modelling approach, the experimental curves are considered to be the results of the simultaneous operation of DRV and DRX processes [27]. Therefore, the difference between the DRV and DRX curves, as illustrated in Fig. 5, can be used to calculate the fraction of dynamic softening attributed to DRX. The DRV flow curve represents the work hardening behavior of the unrecrystallized (pancaked) grains. Further, the DRX is initiated at ε_c and eventually leads to softening on further straining, which is the difference between the σ_{DRV} and σ_{DRX} values. At the point of saturation, we get the saturated stress (σ_{sat}), which

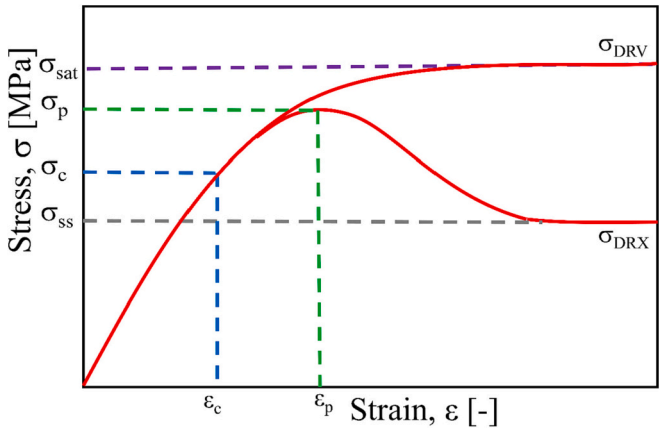

Fig. 5. Schematic illustration of DRV and DRX curves showing the stress/strain parameters used to determine the kinetics using Avrami–equations. σ_{ss}, σ_c, σ_p, and σ_{sat} are the steady-state stress, critical stress for the onset of DRX, peak stress, and saturated stress respectively.

represents the work-hardened grains and therefore the driving force for the continuation of DRX [27]. The DRX volume fraction (X_{DRX1}) can be estimated as:

$$X_{DRX1} = \frac{(\sigma_{sat} - \sigma_p)}{(\sigma_{sat} - \sigma_{ss})} \text{ for } \varepsilon \geq \varepsilon_c \quad (1)$$

where, σ_{ss}, $\sigma_p$and σ_{sat} are the saturated stress, peak stress and steady state-stress respectively, as illustrated in Fig. 5. The numerator ($\sigma_{sat} - \sigma_p$) in the Eq. 1 constitutes the flow softening, whereas the denominator $\sigma_{sat} - \sigma_{ss}$ indicates the maximum achievable softening (Fig. 6).

Furthermore, the X_{DRX} values can also be estimated by an exponent-type Avrami Eq. [27] and can be expressed as:

$$X_{DRX2} = 1 - exp\left[-k\left\{ \frac{(\varepsilon - \varepsilon_c)}{(\varepsilon_p)} \right\}^{n_c} \right] \quad (2)$$

where, k is a constant, n_c is the Avrami exponent and the X_{DRX2} is the volume fraction of DRX evaluated using Eq. 2. Applying natural logarithm to both sides of the Eq. 2 imply:

$$ln\{ -ln(1 - X_{DRX2}) \} = lnK + n_c ln\left\{ \frac{(\varepsilon - \varepsilon_c)}{(\varepsilon_p)} \right\} \quad (3)$$

To estimate the k and n_c values, the $\ln\{-\ln(1 - X_{DRX2})\}$ values were plotted against $ln\left\{\frac{(\varepsilon-\varepsilon_c)}{(\varepsilon_p)}\right\}$ values. For example, a representative plot at 1323 K /10^{-1} s^{-1}, as shown in Fig. 6, enabled estimation of k and n_c values to be about 0.19 and 3.26, respectively. The estimated values of k and n_c at other test conditions are also listed in Table 1. The average values of k and n_c were approximated to be about 0.2 and 3.6, respectively. Therefore, by substituting the average values of k and n_c in Eq. 3, the X_{DRX2} for the $Al_{0.3}$CoCrFeNi HEA can also be expressed, as:

$$X_{DRX2} = 1 - exp\left[-0.2\left\{ \frac{(\varepsilon - \varepsilon_c)}{(\varepsilon_p)} \right\}^{3.6} \right] \quad (4)$$

Further, the predicted X_{DRX2} values (Eq. 4) were plotted together with the X_{DRX1} values (Eq. 2) against true strain, as shown in Figs. 7(a) – (d). It is observed that the Avrami model predicted the DRX volume fractions (X_{DRX2}, plotted as symbols) as a function of true strain very accurately, correlating well with the experimental results (X_{DRX1}, plotted as solid lines). In addition, it is observed from Fig. 7 that the X_{DRX} values increased with the increase in temperature and decrease in strain rate. Therefore, as expected, the degree of DRX increased with lowering of strain rate, resulting in the reduction of flow stress that is quite consistent with the current results (Fig. 2).

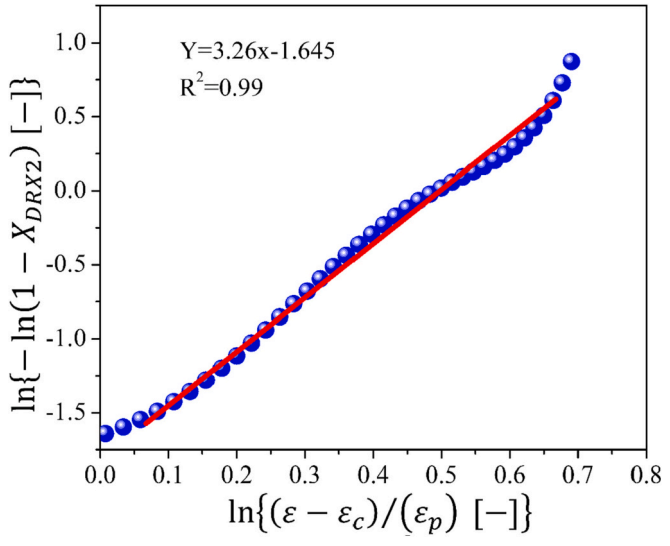

Fig. 6. Linear fitting of $ln\{ -ln(1 - X_{DRX2}) \}$ *vs.*$ln\left\{\frac{(\varepsilon-\varepsilon_c)}{(\varepsilon_p)}\right\}$ for $Al_{0.3}$CoCrFeNi HEA deformed at 1323 K/ $10^{-1}s^{-1}$ enabling estimation of n_c and k values.

When compared with the DRX kinetics of CoCrFeMnNi HEA hot deformed in the temperature and strain rate ranges of 1273–1323 K and 10^{-2}–10^{-1} s^{-1}, respectively [15], the DRX volume fractions of $Al_{0.3}$CoCrFeNi HEA were found to be lower compared to those of CoCrFeMnNi HEA under similar test conditions. This is because the presence of Al in $Al_{0.3}$CoCrFeNi HEA enhances lattice distortion, which consequently reduces the diffusion speed of the solute atoms and vacancies [28]. Therefore, the sluggish diffusion in the $Al_{0.3}$CoCrFeNi HEA due to the presence of Al reduced the migration of dislocations and GBs, thereby retarding the rate of DRX process. Furthermore, in order to create a lattice distortion, a single phase must be stable without any precipitation [29]. In the present case, according to the CALPHAD predictions, the FCC phase was found to be stable for the $Al_{0.3}$CoCrFeNi HEA at temperatures >1373 K [6]. Although, the occurrence of B_2 phase is possible at temperatures <1373 K according to CALPHAD, the short time of hot deformation was not enough to stabilize the B_2 phase. Therefore, it is presumed that $Al_{0.3}$CoCrFeNi HEA samples under the current test conditions comprised essentially of the FCC phase and devoid of any precipitates. Therefore, the lattice distortion caused by the Al enhanced the flow stress values in $Al_{0.3}$CoCrFeNi HEA compared to those of CoCrFeMnNi HEA under similar test conditions [15].

3.4. Microstructural characterization and micro-texture analysis

3.4.1. Initial material

The microstructure of as hot-rolled $Al_{0.3}$CoCrFeNi HEA was examined using the EBSD technique. Figs. 8(a) and (b) depict the inverse pole figure (IPF) and the image quality (IQ) maps, respectively. The Σ3 twin boundaries and LAGBs in the IQ map account for ≈15.2% and ≈ 57% of all the GBs. Further, the microstructure depicted in Figs. 8(a) and (b) essentially comprised of equiaxed grains with an average grain size of ≈ 52 μm (disregarding the Σ3 twin boundaries). Fig. 8 (c) shows the inverse pole figure with a weak texture that is mostly oriented towards <111> fiber with the peak intensity around ≈ 2.14 multiples of uniform density (MUD*).

3.4.2. Effect of temperature and strain rate on the microstructure

The evolution of microstructures in the isothermally compressed $Al_{0.3}$CoCrFeNi HEA samples has been investigated using inverse pole figure (IPF) maps (Fig. 9), image quality (IQ) maps (Fig. 10), grain average misorientation (GAM) maps (Fig. 11), and Kernel average misorientation (KAM) maps (Fig. 12). The average grain size increased with the decrease in strain rate and increase in temperature (Table 2).

In general, an increase in temperature enhances the GB mobility which eventually improves the DRX rate [30]. In addition, it has been assumed that the evolution of substructure influences the formation of DRX nuclei [31]. The rates of DRX nucleation and GB migration can be dynamically balanced by the occurrence of competing thermally activated competing processes, i.e., bulk diffusion and GB diffusion. Further, the interface can be defined as a boundary formed as a result of the generation, recovery and rearrangement of dislocations, and the respective interface migrates only when a specific configuration of the large angle boundary is achieved, i.e., nucleation. DRX involves two competing processes i.e., formation of interface (nucleus) and migration of interface (growth) [32]. When the formation of interface and its migration occurs concurrently, the DRX is driven by the slower of these two processes. If the rate of interface formation is sluggish compared to the rate of migration, then the material should experience certain strain (ε_c in this case), before attaining the critical configuration of the nucleus enabling migration to occur that eventually leads to the softening of the flow stress curve. Additionally, it is known that the DRX mechanisms in low SFE materials is influenced by the presence of Σ3 twin boundaries,

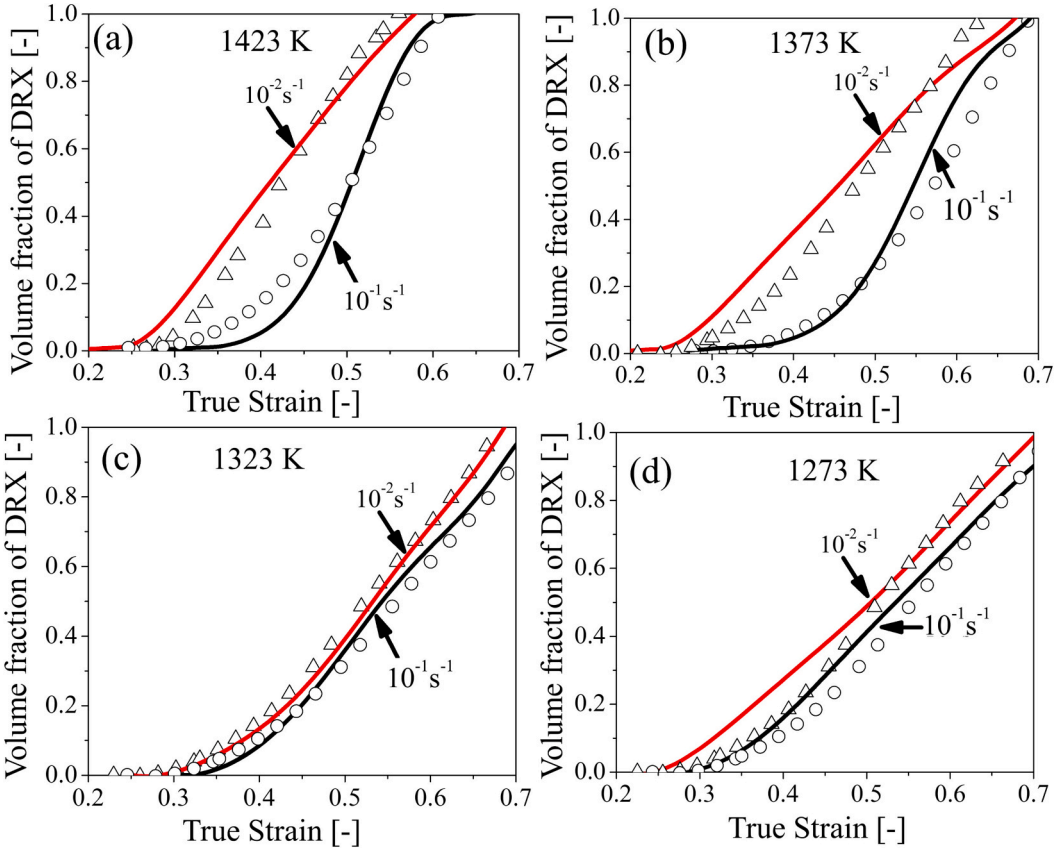

Fig. 7. Plots of X_{DRX1} values (solid lines) as a function of true strain (ε) in comparison with the X_{DRX2} values (symbols) at different temperatures (a) 1423 K, (b) 1373 K, (c) 1323 K and (d) 1273 K for the two strain rates 10^{-2} and 10^{-1} s^{-1}.

where the GB energy is reduced by the formation of Σ3 twin boundaries, enabling enhanced GB mobility [33]. Therefore, an increase in the fraction of Σ3 twin boundaries enhances the kinetics of DRX.

Currently, in the stated test conditions of $Al_{0.3}$CoCrFeNi HEA, the increase in temperature expectedly enhanced the DRX kinetics and as a result, the corresponding strain required to complete the DRX ($X_{DRX} = 1$) decreased, as shown in Fig. 7. For instance, at 10^{-2} s^{-1}, an increase in temperature decreased the strain required to achieve the maximum DRX volume fraction, i.e., $X_{DRX} = 1$, signifying enhanced DRX kinetics. However, the X_{DRX} was found to be <1 at 10^{-1} s^{-1} in the temperature range of 1273–1323 K, (Table 1), signifying the incomplete DRX process. Additionally, the ε_c values for the initiation of DRX, as listed in Table 1, decreased with the increase in temperature and decrease in strain rate. This means that the DRX kinetics were enhanced at lower strain rate (10^{-2} s^{-1}) and at higher temperatures, as the critical configuration to form large angle boundaries (nucleus) can be reached at small strains, as the rate of interface formation becomes faster than rate of migration, due to enhanced recovery and diffusion. Further, it was observed that much higher strains were needed in the case of $Al_{0.3}$CoCrFeNi HEA compared to CoCrFeMnNi HEA [15] to reach similar levels of X_{DRX} values under the imposed test conditions (1273–1373 K/10^{-1}–10^{-2} s^{-1}), and this has been attributed to the addition of Al in $Al_{0.3}$CoCrFeNi HEA, which retarded the DRX rate as a result of sluggish diffusion and lattice distortion effects, as explained in Section 3.3.2.

At 10^{-1} s^{-1}, the increase in deformation temperature decreased the low angle grain boundary (LAGB) fractions, as shown in Table 2. In the entire temperature range (1273–1423 K), nucleation of fine DRX grains was evident through nucleation and growth of a necklace-type microstructure along the GBs of the prior deformed grains, as shown in Figs. 9 (a) – (d). Such formation of DRX grains along the GBs during hot deformation are associated with the discontinuous dynamic recrystallization (DDRX) process [33]. The presence of LAGBs and the high intensity of local misorientations (KAM) along the GBs of the pancaked (prior) grains, as shown in Figs.10(a) – (d) and Figs. 11(a) – (d), respectively, typically represent the evolution of dislocation densities during the hot deformation. The nucleation of fine, recrystallized grains along the GBs of the pancaked grains marked the onset of DRX. In addition, at 10^{-1} s^{-1}, the fraction of Σ3 twin boundaries increased with the increase in deformation temperature, as shown in Figs. 10(a) – (c), and also listed in Table 2. The increase in the fraction of Σ3 twin boundaries further enhanced the occurrence of DRX and thus increased the respective f_{DRX} values (the area fractions of DRX grains (blue color) in the GAM maps, Fig. 12), as listed in Table 2, demonstrating the formation of DRX nuclei via large-scale elimination of dislocations. Accordingly, the LAGB fractions decreased with the increase in deformation temperature.

Furthermore, the average DRX grain size (D_{DRX}) increased with the increase in deformation temperature, varying marginally in the range of ≈ 5.4–16 μm, as listed in Table 2. Eventually, the increase in temperature at 10^{-1} s^{-1} enhanced the DRX rate. On the other hand, the X_{DRX} values realized at 1373 K / 10^{-1} s^{-1} and 1423 K / 10^{-1} s^{-1} reached high levels prior to or near 0.7 strain, although the respective flow curves did not yet reach the steady-state at this strain. This is due to the continuous reconstitution of the microstructure occurring through the evolution of DRX grains. However, at 1423 K/10^{-1} s^{-1}, there was a slight reduction in the D_{DRX}, and f_{DRX}, and correspondingly, a slightly higher LAGB fraction compared to that at 1373 K/10^{-1} s^{-1} (Table 2). This is attributed to the accelerated nucleation and growth of new DRX grains at the higher temperature, i.e., 1423 K (Figs. 10(d), 12(d)).

In the case of $Al_{0.3}$CoCrFeNi HEA samples hot deformed at 1273 K/10^{-2} s^{-1} and 1323 K/10^{-2} s^{-1}, necklace-type recrystallized microstructures were observed along the GBs of the pancaked grains formed as

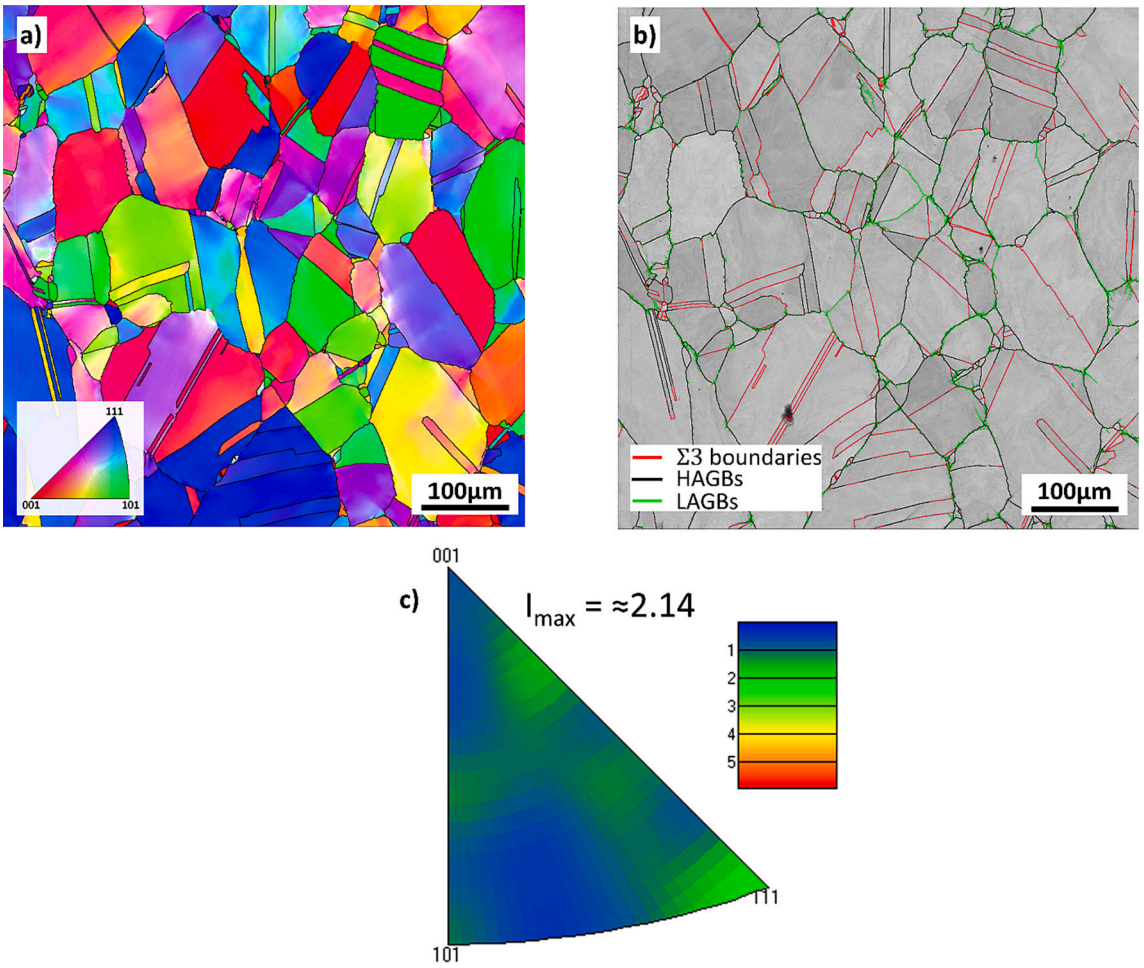

Fig. 8. a) IPF map; b) IQ map; c) inverse pole figure of as hot–rolled $Al_{0.3}CoCrFeNi$ HEA.
*MUD is a probability density that defines the frequency with which any specific texture component occurs.

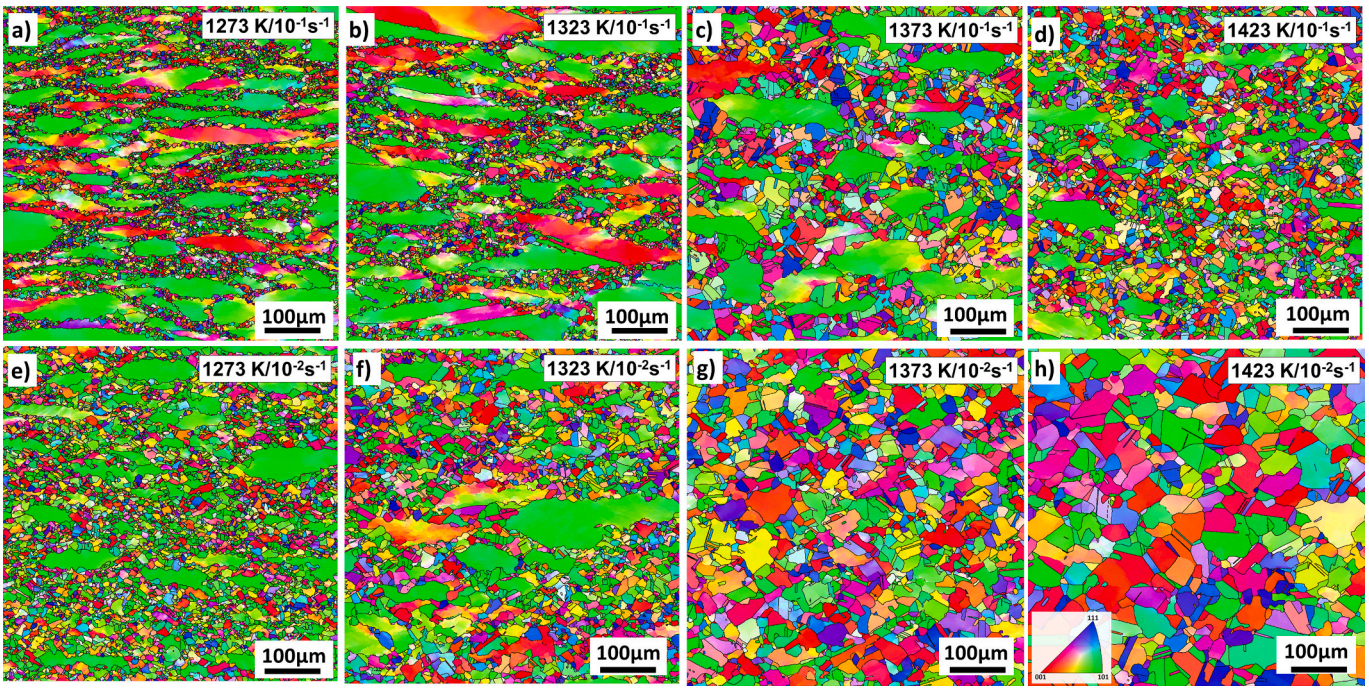

Fig. 9. IPF color maps of $Al_{0.3}CoCrFeNi$ HEA hot deformed at 10^{-1} and 10^{-2} s^{-1} in the temperature range of 1273–1423 K.

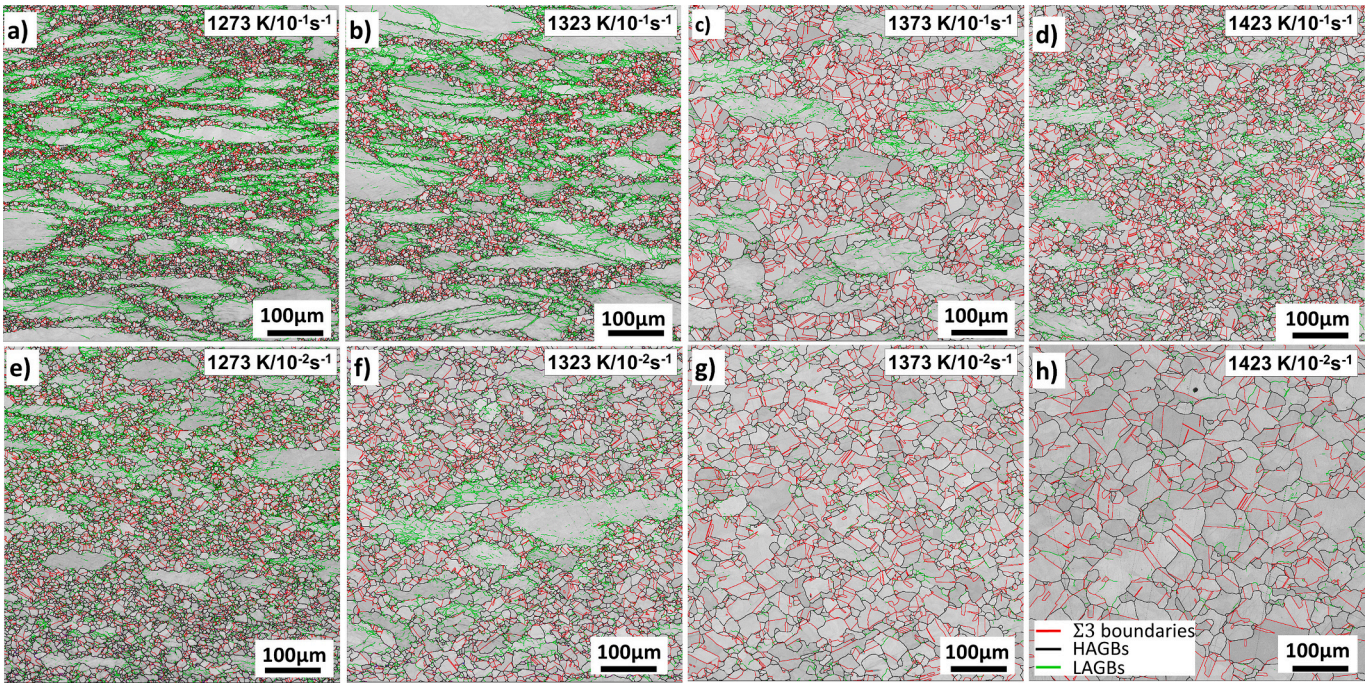

Fig. 10. Image quality (IQ) maps of $Al_{0.3}$CoCrFeNi HEA isothermally compressed in the temperature range 1273–1423 K at the two strain rates 10^{-1} (a – d) and 10^{-2} (e – h) s^{-1}.

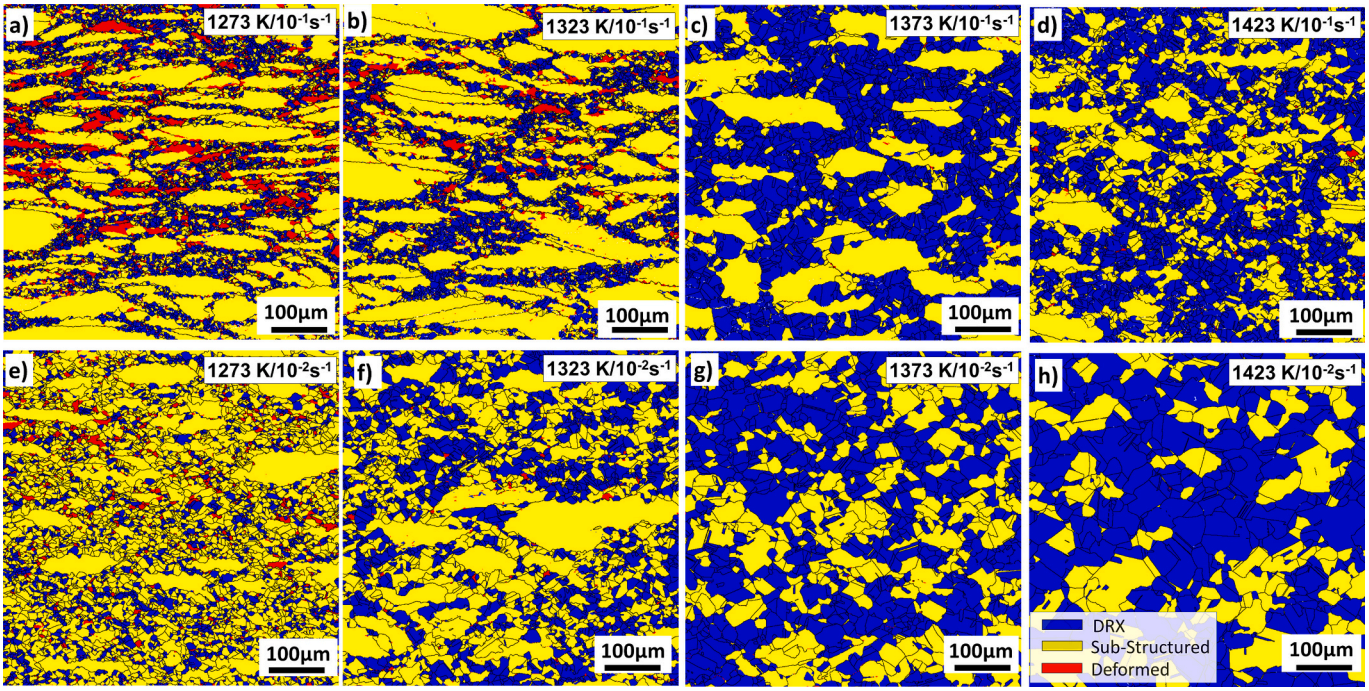

Fig. 11. KAM profile maps of hot deformed $Al_{0.3}$CoCrFeNi HEA in the temperature range 1273–1423 K at the two strain rates 10^{-1} (a – d) and 10^{-2} (e – h) s^{-1}.

a result of the nucleation and growth of DRX grains, as shown in Figs. 10 (e) and (f), respectively. The corresponding KAM profile maps (Figs.11 (e) and (f), respectively) revealed accumulation of dislocations at the GBs of the pancaked grains, which eventually led to the occurrence of DDRX, although there existed a competition between DRX and DRV. The D_{DRX} values at 1273 K/10^{-2} s^{-1} and 1323 K/10^{-2} s^{-1} are ≈ 6.1 and 11 μm, respectively. Further, at 1273 K/10^{-2} s^{-1} and 1323 K/10^{-2} s^{-1}, the X_{DRX} values almost reached a maximum value of unity, as shown in Figs. 7(c) and (d), respectively. In comparison, the corresponding X_{DRX} values of the samples deformed at the same temperatures (1273 and 1323 K), but at the higher strain rate of 10^{-1} s^{-1}, could not reach the maximum level (*i. e*, X_{DRX}<1) at 0.7 strain, as the DRX process was incomplete. This is because of the fact that at lower strain rate, the large angle boundary configurations (nucleus) were achieved at lower ε_c values resulting in enhanced DRX kinetics.

On the other hand, $Al_{0.3}$CoCrFeNi HEA samples deformed at 1373 K/10^{-2} s^{-1} and 1423 K/10^{-2} s^{-1} reached the maximum value of X_{DRX}(i.e., 1), indicating the completion of first DRX cycle and that too at lower

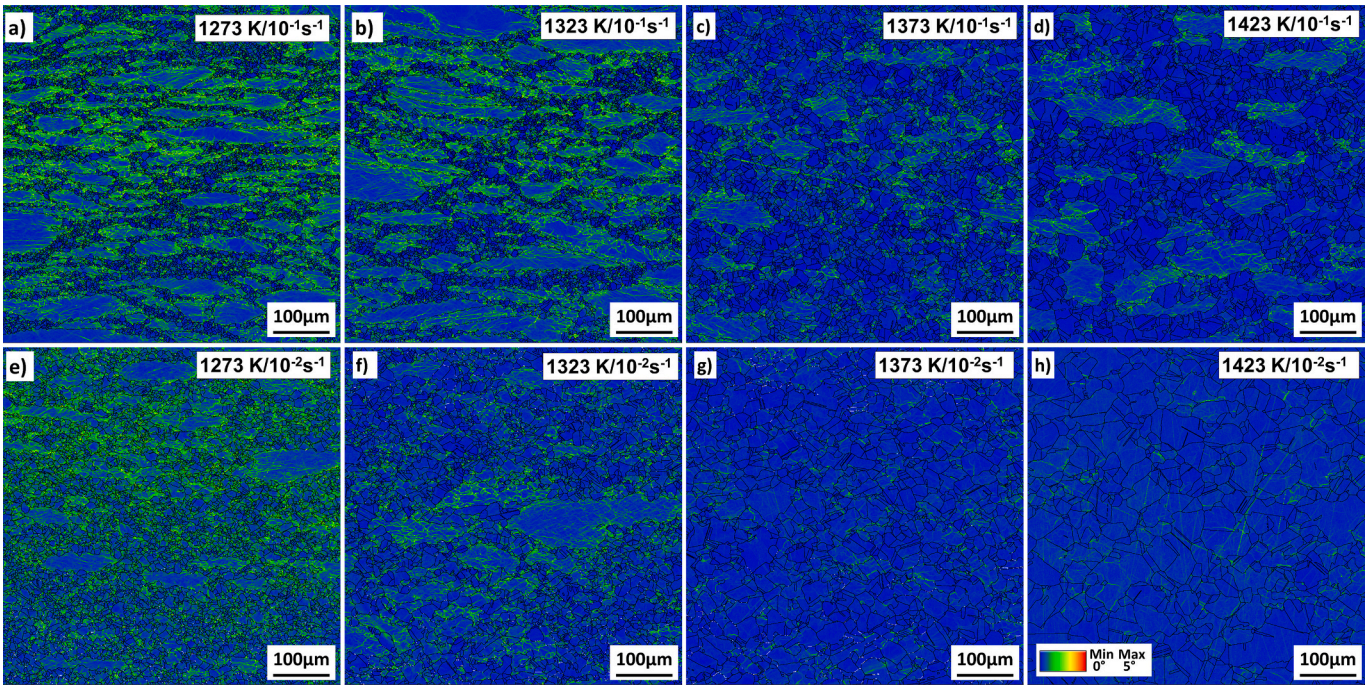

Fig. 12. GAM maps highlighting recrystallized grains (blue color), substructured grains (yellow color) and deformed grains (red color) observed in $Al_{0.3}CoCrFeNi$ HEA hot deformed in the temperature range 1273–1423 K at the two strain rates 10^{-1} (a – d) and 10^{-2} (e – h) s^{-1}. (For interpretation of the references to color in this figure legend, the reader is referred to the web version of this article.)

Table 2
The evolution of grain size following DRX and corresponding fractions of GBs (including twin boundaries) at different test conditions.

Strain rate (s^{-1})	Temperature (K)	Average grain size (D µm)	D_{DRX} (µm)	$D_{unrecrystallized}$ (µm)	Recrystallization area fraction f_{DRX}	HAGBs (%)	LAGBs (%)	Σ3 twin boundaries (%)
10^{-1}	1273	6.22	5.4	7.6	26.8	39.2	60.8	7.6
	1323	7.60	6.8	9.3	27.9	40.4	59.6	10.3
	1373	16.91	16.0	21.0	61.0	65.0	35.0	29.9
	1423	13.01	12.4	14.5	55.4	62.7	37.3	23.0
10^{-2}	1273	9.25	6.1	11.3	20.7	40.5	59.5	9.6
	1323	13.30	11.0	16.9	40.4	54.0	46.0	18.0
	1373	22.25	19.9	28.1	57.8	76.0	24.0	32.6
	1423	32.94	30.4	41.1	66.4	73.8	26.2	33.8

strains compared to those of the samples deformed at higher strain rate 10^{-1} s^{-1} at the same temperatures (1373 K and 1423 K). It is to be noted that the flow curves at 1373 K/10^{-2} s^{-1} and 1423 K/10^{-2} s^{-1}, as shown in Fig. 2(b), displayed continuous flow softening without any steady-state, due to continuous occurrence/progression of dynamic recrystallization. Therefore, the f_{DRX} values at 10^{-2} s^{-1}, as listed in Table 2, increased with the increase in temperature. Likewise, the LAGBs decreased and Σ3 twin boundaries increased with the increase in temperature as listed in Table 2. The increase in the deformation temperature led to the coarsening of DRX grains, e.g., the D_{DRX} values at 1373 K/10^{-2} s^{-1} and 1423 K/10^{-2} s^{-1} were ≈ 19.9 and 30.4 µm, respectively.

It is known that the D_{DRX} is strongly influenced by both the deformation temperature as well as the strain rate. In other words, the Zener-Holloman (Z) parameter has a close relationship with D_{DRX}. In this study, the Z parameter was evaluated at 0.7 strain using a constitutive model describing the flow behavior of $Al_{0.3}CoCrFeNi$ HEA, developed in our previous study [13]. The relationship between the D_{DRX} and Z parameters can be expressed as:

$$D_{DRX} = A_{DRX} \bullet Z^{n_{DRX}} \quad (5)$$

where, A_{DRX} and n_{DRX} are material constants.

Referring to Fig. 13, the relationship between D_{DRX} and Z parameter considering all the D_{DRX} values obtained on the hot deformed specimens

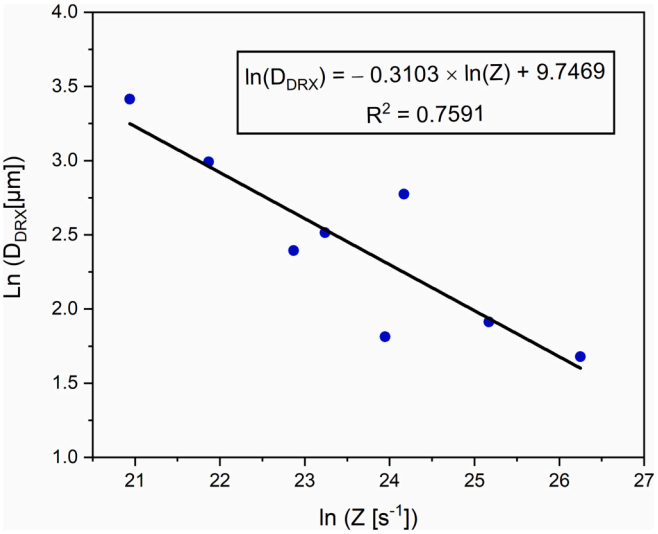

Fig. 13. Relationship between D_{DRX} and Z.

tested in the DRX domain comprising temperature range 1273–1423 K and at the two strain rates (10^{-1} and 10^{-2} s^{-1}), as listed in Table 2, can be expressed as:

$$D_{DRX} = 1.7101 \times 10^4 \bullet \left(Z^{-0.31}\right) \quad (6)$$

Table 3 lists the A_{DRX} and n_{DRX} values of the HEAs studied by the present authors in comparison with those of different steels and superalloys reported in literature. A low value of n_{DRX} for $Al_{0.3}$CoCrFeNi HEA (−0.31) suggests that the Z parameter highly influenced the D_{DRX}. In comparison, the n_{DRX} values of different alloys listed in Table 2, vary in a narrow range (− 0.09 to −0.36) suggesting weak dependence of D_{DRX} on Z parameter. The positive value (0.014) of n_{DRX} for UNS 6617 superalloy [34] remains elusive.

3.4.3. Effect of strain on microstructural evolution

In order to understand the DRX characteristics of $Al_{0.3}$CoCrFeNi HEA, a select test condition of 1323 K/10^{-1} s^{-1} was considered appropriate. As mentioned earlier, a number of samples were isothermally compressed to different strains (≈ 0.2, 0.4 and 0.6) other than the maximum strain (0.7 strain) employed for all the tests, enabling interruption of the test at different strains to understand the progression and mechanisms of DRX in the alloy. The microstructures of these samples deformed to different strains were characterized using the EBSD analysis, in order to understand the accumulated dislocation densities, onset of DRX process and DRX grain growth. The IPF maps of the samples deformed to true strains of 0.2, 0.4, 0.6 and 0.7 are presented in Fig. 14 along with the representative flow stress curve. Further, the evolution of microstructures at different strains were investigated using the IQ maps (Figs. 15 (a) – (d)), KAM maps (Figs. 15 (e) – (h)) and GAM maps (Figs. 15 (i) – (l)).

Initially, at 0.2 ε, which is above the ε_c (0.14), a high density of dislocations was accumulated near the GBs of the prior grains. In this regard, the accumulation of LAGBs (in green color) and the high intensity of KAM, as shown in Figs. 15(a) and (e), respectively, represent the accumulation of dislocations along the GBs of the prior grains. Further, the GBs of the prior grains were distorted, which would become the potential nucleation sites for the occurrence of DRX. These sites with high dislocation densities would eventually be replaced by the new DRX grains. Newly formed fine DRX grains are clearly visible along the GBs of the prior grains in the corresponding GAM map as presented in Fig. 15i, suggesting the onset of DRX process already at the ε_c. At 0.4 ε, i.e., beyond the ε_p = 0.26, flow softening occurred due to the continued formation of DRX grains replacing the dislocations accumulated along the GBs of the prior deformed grains (as shown in Fig. 15f). These strain-free DRX grains were also observed in the GAM map, as shown in Fig. 15 (j). The corresponding X_{DRX} and f_{DRX} values at 0.4 ε were estimated to be about 0.1 and 6.2%, respectively, as can be discerned from Fig. 7(c) and Fig. 15(j). In addition, the Σ3 twin boundaries (red color), which are known to enhance the DRX kinetics, were also observed along the nucleation sites of the DRX grains Fig. 15(b).

On further straining to 0.6 ε, the flow stress curve showed increased softening, whereby the DRX process continued to result in dynamic nucleation and migration of new strain free grains, thereby decreasing the fraction of LAGBs and the density of dislocations generated, as shown in Fig. 15(c) and (g), respectively. Eventually, the volume of DRX grains increased, i.e., the X_{DRX} value and, the f_{DRX} value at this strain (0.6 ε) increased to ≈ 0.6 and 21.3%, respectively, as shown in Fig. 7(c) and Fig. 15(k). Accordingly, the fraction of Σ3 twin boundaries increased to 8.1%, as shown in Fig. 16(c) enhancing the DRX kinetics. Furthermore, deformation to 0.7 ε, resulted in further flow softening, thereby enhancing the DRX rate and volume of DRX grains. It is to be noted that the LAGBs and dislocations accumulated throughout the pancaked grains finally get replaced by the new DRX grains, which also undergo deformation during continued straining. The increase in density of dislocations is reflected in respect of increase in GAM value, where the fraction of deformed grains (red) is increased to ≈ 5%, Fig. 15 (l).

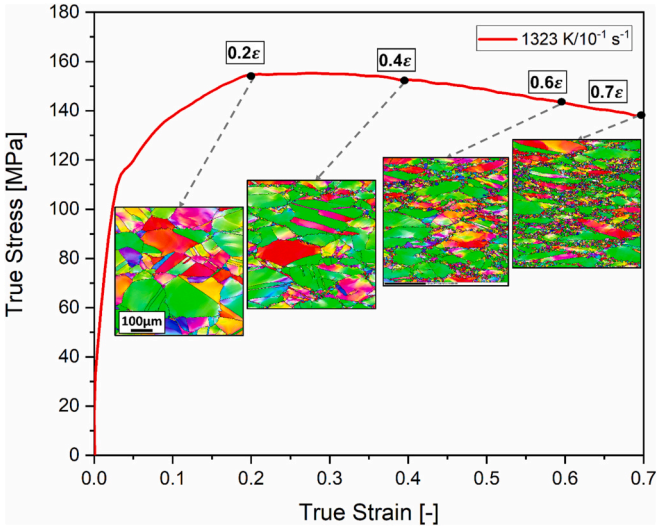

Fig. 14. Microstructural evolution in $Al_{0.3}$CoCrFeNi HEA hot deformed at 1323 K/ 10^{-1} s^{-1} to different true strains of ≈ 0.2, 0.4, 0.6 and 0.7 respectively.

Figure 14 clearly depicts how the continued straining resulted in increased formation of fine DRX grains. As the deformation continued to 0.7 strain, the corresponding X_{DRX} and, the f_{DRX} values reached about ≈ 0.9 and 27.9%, respectively, as shown in Fig. 7(c) and Fig. 15(l). The corresponding fraction of Σ3 twin boundaries increased to 10.3%, as shown in Fig. 15(d). It should be noted that the increments of X_{DRX} and f_{DRX} values with the increase in strain were not in the same range, as they represented the volume and area fractions, respectively. On further straining, the steady-state flow would be achieved marking a dynamic balance between dislocation generation due to continued straining and softening due to dynamic recrystallization. However, in the current test condition, the X_{DRX} value had not yet reached maximum (1), since the flow curve did not show any steady-state. Therefore, the DRX process was incomplete at the calculated strain of 0.7.

Table 3
Dependence of D_{DRX} on the Z parameter for different materials.

Alloy	A_{DRX}	n_{DRX}	References
CoCrFeMnNi	49.15	−0.09	[15]
40Cr steel	668.326	−0.0901	[35]
UNS 6617 superalloy	9.851	0.014	[34]
304 stainless steel	5200	−0.17	[36]
FGH96 superalloy	1730.00	−0.18	[37]
300 M steel	21,000.00	−0.22	[38]
Medium carbon steel LZ50	98,738.00	−0.2956	[39]
UNS N08028 Ni based corrosion resistant alloy	5,610,000	−0.36	[40]
$Al_{0.3}$CoCrFeNi	16,292	−0.31	Current work

3.4.4. Microtextural evolution

In order to characterize the texture evolution, the inverse pole figures (IPFs) were constructed using the acquired EBSD data at different test conditions, as shown in Fig. 1. In this regard, the IPFs are initially evaluated for overall grain as shown in Fig. 16. Further, the grains are partitioned based on the GAM maps as 'recrystallized' grain area fractions (area of blue colored grains in Fig. 12) and 'unrecrystallized' grain area fractions (i.e., the areas of yellow and red colored grains in Fig. 12). The IPFs of the 'recrystallized' grain fractions and the 'unrecrystallized' grain fractions are constructed separately for all the deformation conditions as shown in Figs. 17 and 18, respectively. In addition, the peak MUD (multiples of uniform density) values are shown for each IPF to

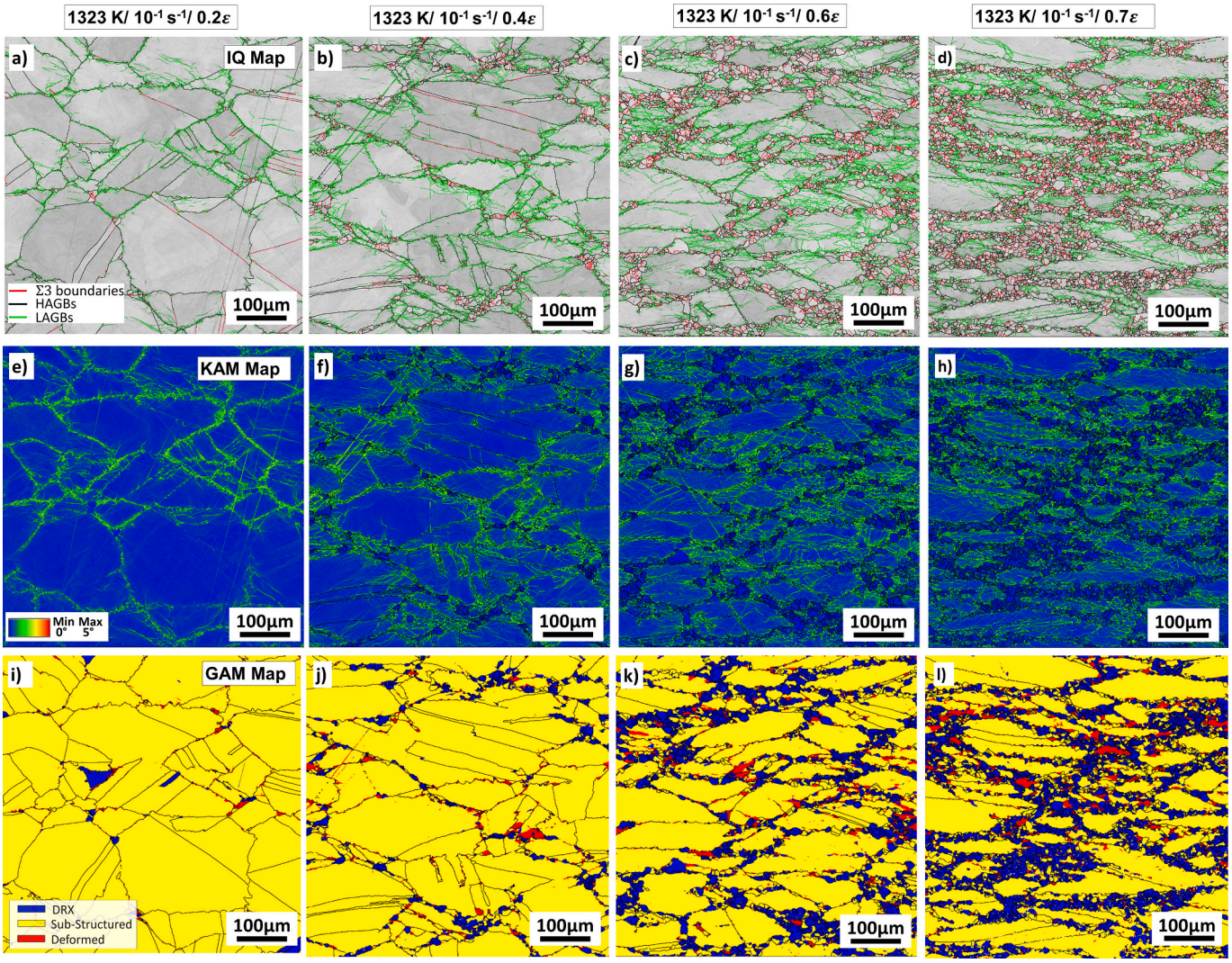

Fig. 15. (a) – (d) IQ maps, (e) – (h) KAM maps, (i) – (l) GAM maps of $Al_{0.3}$CoCrFeNi HEA hot deformed at 1323 K/ 10^{-1} s^{-1} at different strains (≈ 0.2, 0.4, 0.6 and 0.7).

quantify the evolution of the fiber textures. In this regard, the IPF at each deformation condition of the overall grains (Fig. 16) and the recrystallized grains (Fig. 17) depicted weak textures. This was due to the formation of Σ3 twin GBs, which enhanced the formation of DRX grains with random orientations [15,22].

On the other hand, the IPFs of the un-recrystallized grains displayed higher peak MUD values representing a strong deformation texture oriented towards <101> fiber texture, as shown in Fig. 18. A similar behavior of texture evolution in unrecrystallized grains is reported in a hot deformed CoCrFeMnNi FCC HEA [15,22]. Further, an increase in test temperature at 10^{-2} s^{-1}, decreased the peak MUD values of each IPF, as shown in Fig. 18. With increase in the deformation temperature, the volume fraction of the un-recrystallized grains gradually decreased (as listed in Table 3), which eventually resulted in the decrease of the peak MUD values.

On the contrary, the peak MUD values of HEA deformed at 10^{-1} s^{-1} mostly remained steady, in the range of ≈ 4.5–4.9. This is due to the increase in the generation of dislocations at 10^{-1} s^{-1} and therefore, the DRX process was still in active mode. Hence the fraction of unrecrystallized grains increased and contributed to the intensification of the deformation texture as well as the peak MUD values. Further, it should be noted that the peak MUD values in the IPFs of the overall grains are higher than those of the recrystallized grains due to the greater contribution of the texture of dominant unrecrystallized grains. Additionally, it should be noted that in the orientation space, the texture components form during hot compression in the convergent regions of the velocity, i.e., the subgrain and the parent grains finally converged to the same ideal texture component, even though the subgrain formation built up misorientations in the parent grain. In this case of FCC based alloys, the ideal texture component of the deformed grain is <101> component [41].

The IPF maps of the unrecrystallized grains of the hot deformed $Al_{0.3}$CoCrFeNi HEA at 1323 K/ 10^{-1} s^{-1} are also presented as shown in Fig. 19, to understand the texture evolution as a result of increase in strain. Initially, at 0.2ε, the peak MUD value is low with weak texture (Fig. 19) as the generation of dislocations is small, and the prior grains (unrecrystallized grains) are not yet deformed to the extent to evolve into any appreciable texture. Further, at 0.4ε, the prior grains underwent continued deformation, eventually leading to the oriented <101> texture component, thereby increasing the peak MUD. Further increase in strain increased the formation of Σ3 twin boundaries and eventually increased the DRX rate. Therefore, the newly formed DRX grains contributed to the random texture, which effectively reduced the peak MUD values for the IPFs at 0.6 and 0.7ε.

4. Conclusions

Using a Gleeble thermomechanical simulator, the DRX

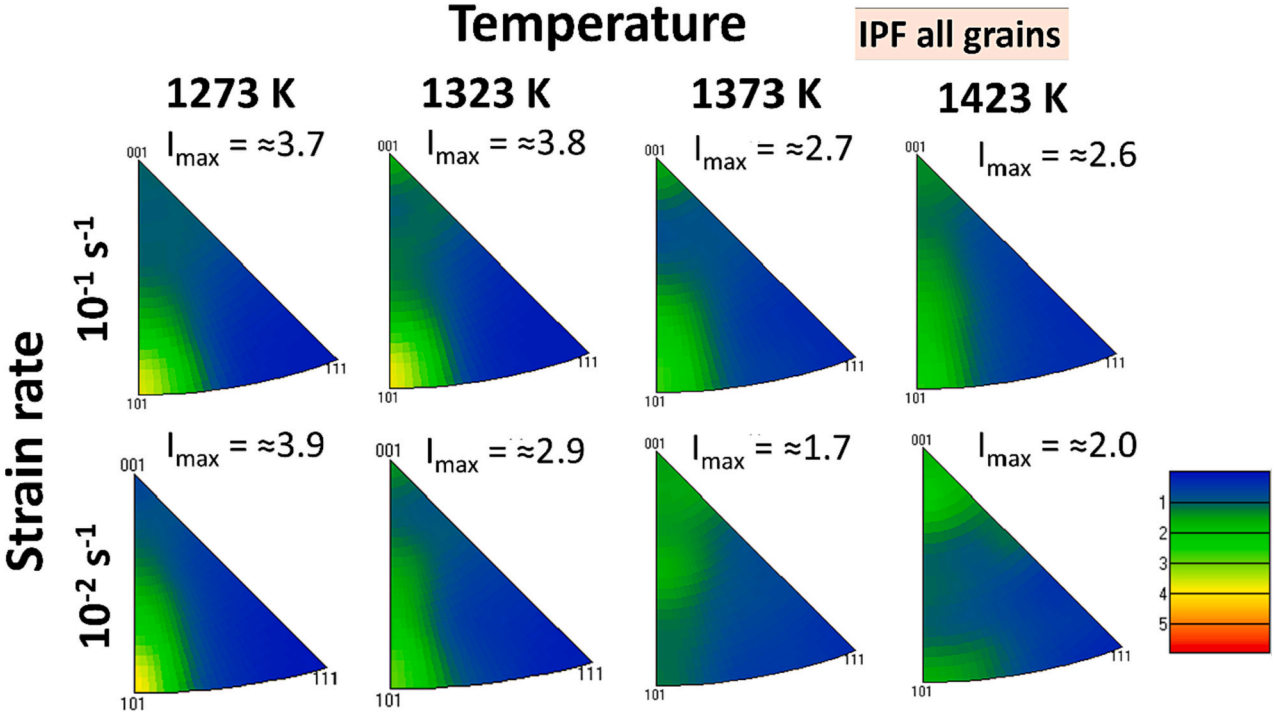

Fig. 16. The IPFs of over all grains obtained at 10^{-1}, 10^{-2} s^{-1} strain rates and temperatures in the range of 1273–1423 K.

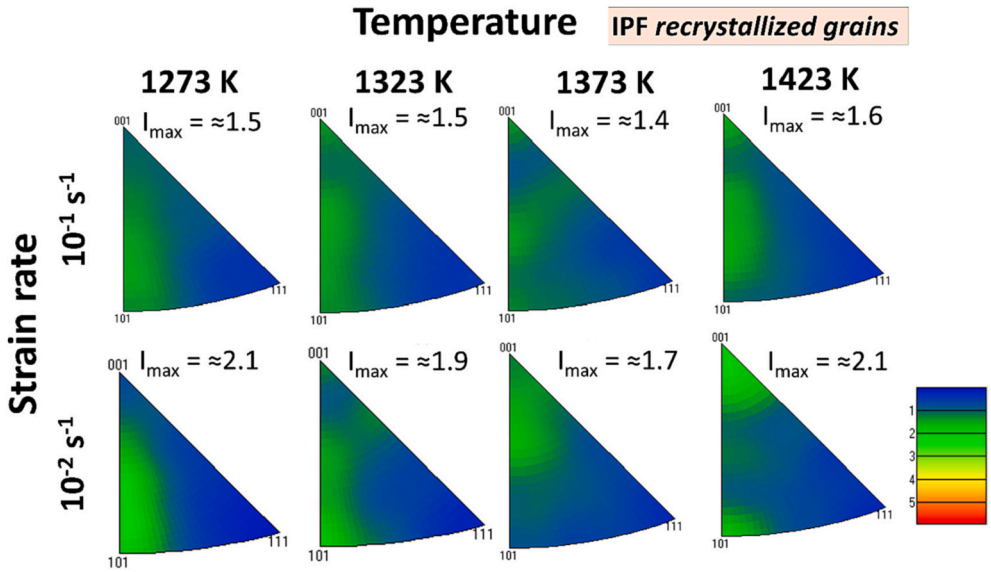

Fig. 17. IPFs of recrystallized (DRX) grains obtained at 10^{-1}, 10^{-2} s^{-1} strain rates and temperatures in the range of 1273–1423 K.

characteristics and kinetics of a Al0.3CoCrFeNi HEA have been investigated by performing hot compression testing in the temperature range of 1273–1423 K, and at two strain rates, 10^{-2} and 10^{-1} s^{-1}. The respective microstructures and micro-textural evolution were analyzed at each deformation condition. In addition, some samples were deformed to different strains at the selected test condition of 1323 K/ 10^{-1} s^{-1} in order to comprehend the evolution and progress of DRX process in the alloy. The following conclusions can be drawn from this study:

Like in other alloy systems, the values of ε_c and ε_p decreased with the increase in deformation temperature and decrease in strain rate, though the values of ε_c were found to be much lower than the corresponding ε_p values.

1. The Avrami-type functions were prudently employed to estimate the values of n_c (3.6) *and* k (0.2) at different deformation conditions to be able to predict the volume fractions of DRX (X_{DRX}).
2. With the increase in deformation temperature from 1273 to 1423 K, the area fractions of DRX grains (f_{DRX}) increased from 26.8 to 61% at 10^{-1} s^{-1} and 20.7–66.4% at 10^{-2} s^{-1} at a true strain of ≈ 0.7
3. DDRX is found to be dominant microstructural mechanism in all the selected test conditions.

The microstructural reconstitution at different strains could be reasonably characterized through EBSD analysis, though very fine grains (below about 80 nm) cannot be discerned due to the limited resolution. Also, a comparison could be made regarding the evolution of

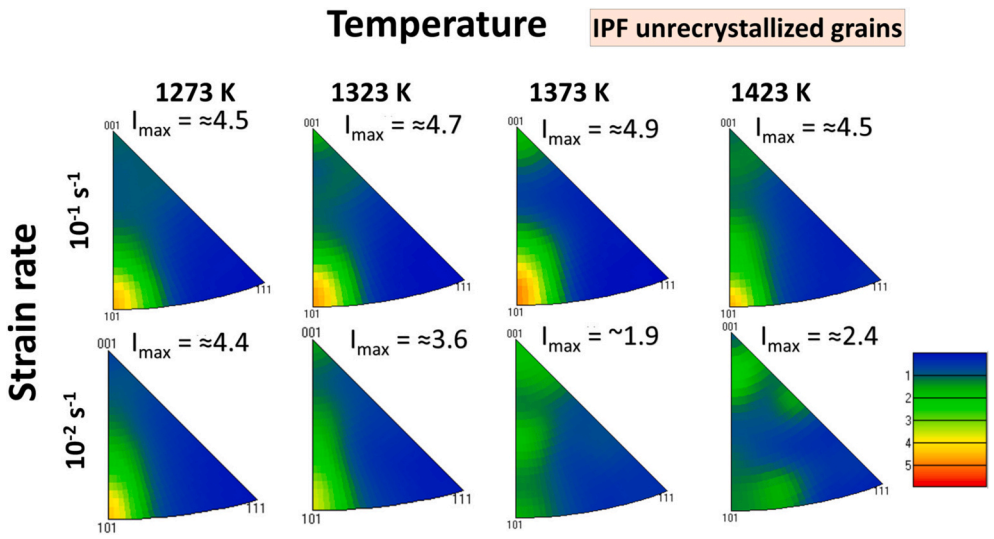

Fig. 18. IPFs of unrecrystallized grains obtained at 10^{-1}, 10^{-2} s^{-1} strain rates and temperatures in the range of 1273–1423 K.

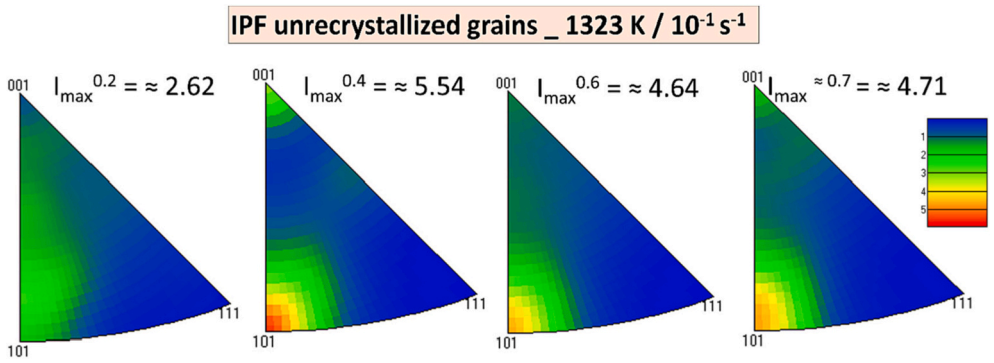

Fig. 19. IPF maps of unrecrystallized grain obtained at 1323 K/ 10^{-1} s^{-1} and strain (a) 0.2, (b) 0.4, (c) 0.6 and (d) 0.7.

DRX grains in respect of the calculated X_{DRX}.

4. Interruption of hot compression testing to different strains enabled comprehending the progression of DRX, which was further corroborated with the evolved microstructures.
5. The microtextural evolution revealed that the IPF maps shows the deformation grains are mostly oriented towards <101> fiber texture due to hot compression.

Declaration of Competing Interest

The authors declare that they have no known competing financial interests or personal relationships that could have appeared to influence the work reported in this paper.

Data availability

Original data will be made available by the authors on request.

Acknowledgement

Authors acknowledge TUNI Foundation as a part of Tampere university's graduate school, Ella and Georg Ehrnrooth foundation, and Walter Ahlström foundation for the financial support. In addition, this work used the facilities of Tampere Microscopy Centre facilities, Tampere University. The authors sincerely thank Juha Uusitalo and Jussi Paavola of University of Oulu for conducting the Gleeble experiments and laboratory rolling, respectively.

References

[1] J.W. Yeh, S.K. Chen, S.J. Lin, J.Y. Gan, T.S. Chin, T.T. Shun, et al., Nanostructured high-entropy alloys with multiple principal elements: novel alloy design concepts and outcomes, Adv. Eng. Mater. 6 (2004) 299–303, https://doi.org/10.1002/adem.200300567.
[2] B. Cantor, I.T.H. Chang, P. Knight, A.J.B. Vincent, Microstructural development in equiatomic multicomponent alloys, Mater. Sci. Eng. A 375–377 (2004) 213–218, https://doi.org/10.1016/j.msea.2003.10.257.
[3] Z. Li, A. Ludwig, A. Savan, H. Springer, D. Raabe, Combinatorial metallurgical synthesis and processing of high-entropy alloys, J. Mater. Res. 33 (2018) 3156–3169, https://doi.org/10.1557/jmr.2018.214.
[4] J. Li, H. Yang, W.Y. Wang, H. Kou, J. Wang, Thermal–mechanical processing and strengthen in AlxCoCrFeNi high-entropy alloys, Front. Mater. (2021) 7, https://doi.org/10.3389/fmats.2020.585602.
[5] W.R. Wang, W.L. Wang, S.C. Wang, Y.C. Tsai, C.H. Lai, J.W. Yeh, Effects of Al addition on the microstructure and mechanical property of AlxCoCrFeNi high-entropy alloys, Intermetallics 26 (2012) 44–51, https://doi.org/10.1016/j.intermet.2012.03.005.
[6] B. Gwalani, V. Soni, M. Lee, S. Mantri, Y. Ren, R. Banerjee, Optimizing the coupled effects of hall-Petch and precipitation strengthening in a Al 0.3 CoCrFeNi high entropy alloy, Mater. Des. 121 (2017) 254–260, https://doi.org/10.1016/j.matdes.2017.02.072.
[7] X. Wang, Z. Zhang, Z. Wang, X. Ren, Microstructural evolution and tensile properties of Al0.3CoCrFeNi high-entropy alloy associated with B2 precipitates, Materials 15 (2022) 1215, https://doi.org/10.3390/ma15031215.
[8] S. Muskeri, B. Gwalani, S. Jha, A. Yu, P.A. Jannotti, R.S. Haridas, et al., Excellent ballistic impact resistance of Al0.3CoCrFeNi multi-principal element alloy with unique bimodal microstructure, Sci. Rep. 11 (2021) 22715, https://doi.org/10.1038/s41598-021-02209-y.
[9] S. Xie, J. Zhang, R. Li, T. Yuan, M. Zhang, M. Wang, et al., Accelerated precipitation of the B2 particles and its effect on Al0.3CoCrFeNi high-entropy alloy by electric

current assisted annealing, Mater. Charact. 181 (2021), 111434, https://doi.org/10.1016/j.matchar.2021.111434.
[10] S. Dasari, A. Sarkar, A. Sharma, B. Gwalani, D. Choudhuri, V. Soni, et al., Recovery of cold-worked Al0.3CoCrFeNi complex concentrated alloy through twinning assisted B2 precipitation, Acta Mater. 202 (2021) 448–462, https://doi.org/10.1016/J.ACTAMAT.2020.10.071.
[11] K. Liu, M. Komarasamy, B. Gwalani, S. Shukla, R.S. Mishra, Fatigue behavior of ultrafine grained triplex Al0.3CoCrFeNi high entropy alloy, Scr. Mater. 158 (2019) 116–120, https://doi.org/10.1016/j.scriptamat.2018.08.048.
[12] M. Patnamsetty, M.C. Somani, S. Ghosh, S. Ahmed, P. Peura, Processing map for controlling microstructure and unraveling various deformation mechanisms during hot working of CoCrFeMnNi high entropy alloy, Mater. Sci. Eng. A 793 (2020), 139840, https://doi.org/10.1016/j.msea.2020.139840.
[13] M. Patnamsetty, S. Ghosh, M.C. Somani, P. Peura, Characterization of hot deformation behavior of Al0.3CoCrFeNi high-entropy alloy and development of processing map, J. Alloys Compd. 914 (2022), 165341, https://doi.org/10.1016/J.JALLCOM.2022.165341.
[14] E.I. Poliak, J.J. Jonas, A one-parameter approach to determining the critical conditions for the initiation of dynamic recrystallization, Acta Mater. 44 (1996) 127–136, https://doi.org/10.1016/1359-6454(95)00146-7.
[15] S. Ghosh, M. Patnamsetty, M.C. Somani, P. Peura, Characteristics of dynamic softening during high temperature deformation of CoCrFeMnNi high-entropy alloy and its correlation with the evolving microstructure and micro-texture, J. Mater. Res. Technol. 15 (2021) 6608–6623, https://doi.org/10.1016/j.jmrt.2021.11.089.
[16] F.J. Humphreys, M. Hatherly, Chapter 13 - Hot deformation and dynamic restoration, in: F.J. Humphreys (Ed.), Hatherly MBT-R and RAP, Second E, Elsevier, Oxford, 2004, https://doi.org/10.1016/B978-008044164-1/50017-7, p. 415–V.
[17] A.J. Zaddach, R.O. Scattergood, C.C. Koch, Tensile properties of low-stacking fault energy high-entropy alloys, Mater. Sci. Eng. A 636 (2015) 373–378, https://doi.org/10.1016/j.msea.2015.03.109.
[18] F. He, Z. Wang, B. Han, Q. Wu, D. Chen, J. Li, et al., Solid solubility, precipitates, and stacking fault energy of micro-alloyed CoCrFeNi high entropy alloys, J. Alloys Compd. 769 (2018) 490–502, https://doi.org/10.1016/J.JALLCOM.2018.07.336.
[19] M. Beyramali Kivy, Zaeem M. Asle, Generalized stacking fault energies, ductilities, and twinnabilities of CoCrFeNi-based face-centered cubic high entropy alloys, Scr. Mater. 139 (2017) 83–86, https://doi.org/10.1016/j.scriptamat.2017.06.014.
[20] B. Gwalani, S. Gorsse, D. Choudhuri, M. Styles, Y. Zheng, R.S. Mishra, et al., Modifying transformation pathways in high entropy alloys or complex concentrated alloys via thermo-mechanical processing, Acta Mater. 153 (2018) 169–185, https://doi.org/10.1016/J.ACTAMAT.2018.05.009.
[21] N. Haghdadi, S. Primig, M. Annasamy, P. Cizek, P.D. Hodgson, D.M. Fabijanic, On the hot-worked microstructure of a face-centered cubic Al0.3CoCrFeNi high entropy alloy, Scr. Mater. 178 (2020) 144–149, https://doi.org/10.1016/j.scriptamat.2019.11.022.
[22] R.R. Eleti, T. Bhattacharjee, L. Zhao, P.P. Bhattacharjee, N. Tsuji, Hot deformation behavior of CoCrFeMnNi FCC high entropy alloy, Mater. Chem. Phys. 210 (2018) 176–186, https://doi.org/10.1016/j.matchemphys.2017.06.062.
[23] F.J. Humphreys, M. Hatherly, Recovery and recrystallization DURING AND after hot deformation. Recrystallization and Related Annealing Phenomena, 1995, pp. 363–392, https://doi.org/10.1016/B978-0-08-041884-1.50018-0.
[24] D.-X. Wen, Y.C. Lin, H.-B. Li, X.-M. Chen, J. Deng, L.-T. Li, Hot deformation behavior and processing map of a typical Ni-based superalloy, Mater. Sci. Eng. A 591 (2014) 183–192, https://doi.org/10.1016/j.msea.2013.09.049.
[25] N.N. Guo, L. Wang, L.S. Luo, X.Z. Li, R.R. Chen, Y.Q. Su, et al., Hot deformation characteristics and dynamic recrystallization of the MoNbHfZrTi refractory high-entropy alloy, Mater. Sci. Eng. A 651 (2016) 698–707, https://doi.org/10.1016/j.msea.2015.10.113.
[26] H.J. McQueen, N.D. Ryan, Constitutive analysis in hot working, Mater. Sci. Eng. A 322 (2002) 43–63, https://doi.org/10.1016/S0921-5093(01)01117-0.
[27] J.J. Jonas, X. Quelennec, L. Jiang, É. Martin, The Avrami kinetics of dynamic recrystallization, Acta Mater. 57 (2009) 2748–2756, https://doi.org/10.1016/j.actamat.2009.02.033.
[28] J. Wang, H. Li, H. Yang, Y. Zhang, W.Y. Wang, J. Li, Hot deformation and subsequent annealing on the microstructure and hardness of an Al0.3CoCrFeNi high-entropy alloy, Acta Metall. Sin. (Engl. Lett.) 34 (2021) 1527–1536, https://doi.org/10.1007/s40195-021-01251-z.
[29] H. Oh, D. Ma, G. Leyson, B. Grabowski, E. Park, F. Körmann, et al., Lattice distortions in the FeCoNiCrMn high entropy alloy studied by theory and experiment, Entropy 18 (2016) 321, https://doi.org/10.3390/e18090321.
[30] S. Mandal, M. Jayalakshmi, A.K. Bhaduri, Sarma V. Subramanya, Effect of strain rate on the dynamic recrystallization behavior in a nitrogen-enhanced 316L(N), Metall. Mater. Trans. A: Phys. Metall. Mater. Sci. (2014), https://doi.org/10.1007/s11661-014-2480-1.
[31] F.J. Humphreys, M. Hatherly, Chapter 14 - continuous recrystallization during and after large strain deformation, in: F.J. Humphreys (Ed.), Hatherly MBT-R and RAP, Second E, Elsevier, Oxford, 2004, pp. 451–467, https://doi.org/10.1016/B978-008044164-1/50018-9.
[32] N. Ravichandran, Y.V.R.K. Prasad, Dynamic recrystallization during hot deformation of aluminum: A study using processing maps, Metall. Trans. A. 22 (1991) 2339–2348, https://doi.org/10.1007/BF02665000.
[33] K. Huang, R.E. Logé, A review of dynamic recrystallization phenomena in metallic materials, Mater. Des. 111 (2016) 548–574, https://doi.org/10.1016/j.matdes.2016.09.012.
[34] G.E. Kodzhaspirov, M.I. Terentyev, Modeling the dynamically recrystallized grain size evolution of a superalloy, Mater. Phys. Mech. 13 (2012) 84.
[35] L. Chen, W. Sun, J. Lin, G. Zhao, G. Wang, Modelling of constitutive relationship, dynamic recrystallization and grain size of 40Cr steel during hot deformation process, Res. Phys. 12 (2019) 784–792, https://doi.org/10.1016/j.rinp.2018.12.046.
[36] A. Dehghan-Manshadi, M.R. Barnett, P.D. Hodgson, Hot deformation and recrystallization of austenitic stainless steel: part I. dynamic recrystallization, Metall. Mater. Trans. A 39 (2008) 1359–1370, https://doi.org/10.1007/s11661-008-9512-7.
[37] H. Wu, M. Liu, Y. Wang, Z. Huang, G. Tan, L. Yang, Experimental study and numerical simulation of dynamic recrystallization for a FGH96 superalloy during isothermal compression, J. Mater. Res. Technol. 9 (2020) 5090–5104, https://doi.org/10.1016/j.jmrt.2020.03.026.
[38] Y.G. Liu, M.Q. Li, J. Luo, The modelling of dynamic recrystallization in the isothermal compression of 300M steel, Mater. Sci. Eng. A (2013), https://doi.org/10.1016/j.msea.2013.03.011.
[39] S. Du, S. Chen, J. Song, Y. Li, Hot deformation behavior and dynamic recrystallization of medium carbon LZ50 steel, Metall. Mater. Trans. A 48 (2017) 1310–1320, https://doi.org/10.1007/s11661-016-3938-0.
[40] L. Wang, F. Liu, H. Chen, Q. Chi, Hot deformation characteristics and kinetics analysis for Ni-based corrosion resistant alloy, Eng. Reports (2021) 3, https://doi.org/10.1002/eng2.12323.
[41] L.S. Tóth, Y. Estrin, R. Lapovok, C. Gu, A model of grain fragmentation based on lattice curvature, Acta Mater. (2010), https://doi.org/10.1016/j.actamat.2009.11.020.